Glucose Hypometabolism Prompts RAN Translation and Exacerbates C9orf72-related ALS/FTD Phenotypes

A.T. Nelson[1], M.E. Cicardi[1], S.S. Markandaiah[1], J. Han[2], N. Philp[2], E. Welebob[1], A.R. Haeusler[1], P. Pasinelli[1], G. Manfredi[3], H. Kawamata[3] and D. Trotti[1]

[1]Weinberg ALS Center, Vickie and Jack Farber Institute for Neuroscience, Department of Neuroscience, Thomas Jefferson University, Philadelphia, PA 19107, USA;
[2]Department of Pathology and Genomic Medicine, Thomas Jefferson University, Philadelphia, PA 19107, USA;
[3]Feil Family Brain and Mind Research Institute, Weill Cornell Medicine, 407 East 61st Street, New York, New York 10065, USA.

Running Title: **Brain Glucose and C9orf72-ALS/FTD**

Correspondence:
Davide Trotti, Ph.D.
Jefferson Hospital for Neuroscience building, 4th floor, room 416
900 Walnut Street, Philadelphia, PA 19107, USA
Tel. 215.955.8416
Email davide.trotti@jefferson.edu

Abstract

The most prevalent genetic cause of both amyotrophic lateral sclerosis and frontotemporal dementia is a $(GGGGCC)_n$ nucleotide repeat expansion (NRE) occurring in the first intron of the *C9orf72* gene (C9). Brain glucose hypometabolism is consistently observed in C9-NRE carriers, even at pre-symptomatic stages, although its potential role in disease pathogenesis is unknown. Here, we identified alterations in glucose metabolic pathways and ATP levels in the brain of asymptomatic C9-BAC mice. We found that, through activation of the GCN2 kinase, glucose hypometabolism drives the production of dipeptide repeat proteins (DPRs), impairs the survival of C9 patient-derived neurons, and triggers motor dysfunction in C9-BAC mice. We also found that one of the arginine-rich DPRs (PR) can directly contribute to glucose metabolism and metabolic stress. These findings provide a mechanistic link between energy imbalances and C9-ALS/FTD pathogenesis and support a feedforward loop model that opens several opportunities for therapeutic intervention.

Key words: ALS/C9orf72/Dipeptide Repeat Proteins/FTD/Glucose Hypometabolism/RAN Translation

Introduction

Amyotrophic lateral sclerosis (ALS) is a progressive adult-onset neurodegenerative disease characterized by the loss of upper and lower motor neurons, leading to muscle wasting, paralysis, and eventually death (Hardiman *et al*, 2017). It is a highly heterogeneous disease with numerous known genetic causes (Hardiman *et al.*, 2017). The most common of these is a $(GGGGCC)_n$ (G_4C_2) nucleotide repeat expansion (NRE) in a non-coding region of the *C9orf72* gene (C9), which accounts for up to 20% of all ALS cases, as well as a subset of frontotemporal dementia (FTD) cases (DeJesus-Hernandez *et al*, 2011; Renton *et al*, 2011).

Common features of various forms of ALS and other neurodegenerative diseases include altered metabolism and bioenergetic homeostasis (Cunnane *et al*, 2020; Nelson & Trotti, 2022). Specifically, ALS patients often exhibit systemic hypermetabolism, mitochondrial dysfunction, and brain glucose hypometabolism (De Vocht *et al*, 2020; Fayemendy *et al*, 2021; Popuri *et al*, 2021; Smith *et al*, 2019). Targeting these alterations through various metabolic treatments and dietary manipulations has shown promise as a potential therapeutic strategy (Beghi *et al*, 2013; Ludolph *et al*, 2020). Furthermore, in C9-NRE carriers, metabolic alterations – especially glucose hypometabolism – can manifest many years before symptom onset (Popuri *et al.*, 2021; Xia *et al*, 2023). Therefore, energy imbalance is an early manifestation in C9-NRE carriers. However, whether it plays a role in disease pathogenesis is unknown.

A well-established pathogenic mechanism associated with C9-ALS/FTD is the aberrant production of dipeptide repeats (DPRs) through repeat-associated non-ATG (RAN) translation. Due to bidirectional transcription of the NRE, five distinct DPRs are produced, including poly-glycine-alanine (GA) and poly-glycine-arginine (GR) from the sense (G_4C_2) transcript; poly-proline-alanine (PA) and poly-proline-arginine (PR) from the antisense (C_4G_2) transcript; and poly-glycine-proline (GP) from both transcripts (Ash *et al*, 2013; Mori *et al*, 2013; Zu *et al*, 2013). Accumulation of DPRs in aggregated forms has been detected in the central nervous system (CNS) of ALS/FTD patients (Ash *et al.*, 2013; Mori *et al.*, 2013). Moreover, the GA, GR, and PR species are toxic in both cultured neurons and *in vivo* (Hao *et al*, 2019; Jensen *et al*, 2020; Kwon *et al*, 2014; May *et al*, 2014; Verdone *et al*, 2022; Wen *et al*, 2014). For these reasons, DPR production and accumulation are thought to directly contribute to neurodegeneration in C9 patients. Still, a complete understanding of the RAN translation mechanism – including how it can be triggered or modified by other disease-related events (such as energy imbalance) – is lacking.

Remarkably, several brain regions that are hypometabolic in C9-NRE carriers – including the frontal and temporal cortices – also tend to be rich in DPR pathology (Ash *et al.*, 2013; De Vocht *et al.*, 2020; Popuri *et al.*, 2021; Schludi *et al*, 2015), which raises the possibility that glucose hypometabolism and DPR formation are mechanistically linked. Notably, cellular stress can selectively enhance RAN translation through activation of the integrated stress response (ISR) (Cheng *et al*, 2018; Green *et al*, 2017; Westergard *et al*, 2019), and glucose deprivation is a well-established activator of the ISR (Pakos-Zebrucka *et al*, 2016; Yang *et al*, 2000; Yang *et al*, 2013). Therefore, we hypothesized that glucose hypometabolism could enhance DPR production in C9-ALS/FTD. However, the reverse hypothesis that DPRs can contribute to glucose hypometabolism is also worth considering. Notably, pathogenic proteins associated with several other neurodegenerative diseases (including amyloid-beta and polyglutamine-expanded Huntingtin, linked to Alzheimer's disease and Huntington's disease, respectively) can interfere with neuronal glucose uptake (Li *et al*, 2012; Prapong *et al*, 2002). Therefore, we also propose that the C9-linked DPRs could act similarly and contribute to or exacerbate metabolic stress.

In the present study, we investigated the brain metabolite profile of asymptomatic BAC transgenic mice carrying the C9orf72-linked repeat expansion (C9-BAC). We identified significant alterations in glucose metabolic pathways and impairment in steady-state brain ATP levels. We then demonstrated that glucose hypometabolism promotes DPR production and impacts the typical survival profile of cultured neurons expressing the C9-NRE *via* activation of the GCN2 arm of the ISR. We also found that chronic exposure of the C9-BAC mouse to glucose hypometabolism exacerbates the production of DPRs and causes motor dysfunction. And finally, we show that PR can impair neuronal glucose uptake, reduce metabolic flux, and activate the ISR. Our results support a feedforward loop linking glucose hypometabolism, cellular stress, and DPR formation, opening several therapeutic intervention opportunities.

Results

Energy metabolites are altered in the C9orf72 BAC mouse brain

Since glucose is classically considered the primary energy substrate in the brain (Dienel, 2019), we hypothesized that reductions in brain glucose uptake (as seen in C9orf72-ALS/FTD patients (De Vocht *et al.*, 2020; Popuri *et al.*, 2021)) would be accompanied by altered brain energy production. Ideally, this would be assessed by measuring metabolite levels directly in patient postmortem tissue. However, this is unfeasible, mainly due to metabolite degradation during the postmortem interval (Chighine *et al*, 2021). Therefore, we leveraged a C9-BAC transgenic mouse model, which carries the entire human C9orf72 gene with a [GGGGCC] repeat expansion (**Fig. EV1A**) and displays C9orf72-related pathology (i.e., RNA foci and DPR inclusions) but otherwise lacks overt behavioral phenotypes (O'Rourke *et al*, 2015). We performed targeted liquid chromatography-mass spectrometry (LC-MS)-based metabolite profiling to measure the abundance of >200 different metabolites in the frontal cortex of both C9-BAC animals and wild-type littermate controls (**Figure 1A; Table EV1**). Principal component analysis (PCA) indicated that the relative differences in this metabolite panel were sufficient in separating C9-BAC from wild-type (**Figure 1B**). Remarkably, out of all metabolites analyzed, ATP was the most significantly altered and was decreased by ~2-fold in C9-BAC brain (frontal cortex) relative to wild-type; ATP:ADP and ATP:AMP ratios were also significantly reduced (**Figure 1C; Table EV1**). Such an ATP imbalance could be explained by dysfunction of the two main energy-producing metabolic pathways: **1)** glycolysis and **2)** oxidative phosphorylation (Dienel, 2019). Interestingly, we observed alterations to both of these pathways in the brain of C9-BAC animals. Enrichment analysis indicated glycolysis was one of the most significantly enriched metabolite categories and decreased in the C9-BAC brain (**Figure 1D**). Upon closer analysis, despite no differences in brain glucose levels (**Figure EV1B**), we observed significant alterations in the glycolytic intermediates glucose-6-phosphate (G6P), glyceraldehyde-3-phosphate (GADP), and phosphoenolpyruvate (PEP) in the frontal cortex of the C9-BAC mice (**Figure 1E**), which indicates that glycolytic function may be altered. We also observed an enrichment of citric acid cycle metabolites (decreased in C9; **Figure 1D**) and a decrease specifically in α-ketoglutarate, a rate-limiting intermediate of the citric acid cycle and precursor for several amino acids, including glutamate (Wu *et al*, 2016) (**Figure EV1C**). Interestingly, C9-BAC animals also showed *higher* levels of several amino acids, including lysine, isoleucine, cysteine, and ornithine (**Figure EV1D**), as well as significant enrichment of metabolite sets involved in amino acid metabolism (**Figure 1D**). This could reflect a compensatory shift towards increased metabolism or transport of amino acids for energy production. Finally, we detected significant decreases in the key redox cofactors NAD^+ and $NADP^+$ in C9-BAC animals with no changes in their reduced counterparts (NADH and NADPH, respectively; **Figure 1F, Figure EV1E**), indicating a hyper-reduced redox state, which could contribute to glycolytic inefficiency by limiting the pool of available NAD^+. We also detected a decrease in the levels of nicotinamide mononucleotide (NMN; **Figure 1F**), which is an essential precursor of NAD^+ (Xie *et al*, 2020), suggesting a potential defect in NAD^+ biosynthesis. Overall, our metabolomics data indicate that the C9orf72 repeat expansion mutation is sufficient to alter ATP levels and the NAD^+/NADH ratio in the mouse frontal cortex.

Glucose hypometabolism drives dipeptide repeat accumulation by enhancing RAN translation

We next evaluated the potential impact of energy imbalance on a pathogenic mechanism of C9-ALS/FTD: the production of DPRs by RAN translation of the C9-NRE (Mori *et al.*, 2013; Zu *et al.*, 2013). Given our observations of glycolytic imbalance in the frontal cortex of the C9-BAC mouse, as well as the known overlap between the brain distribution of DPR-positive inclusions (Ash *et al.*, 2013; Schludi *et al.*, 2015) and brain glucose hypometabolism in human mutation carriers (De Vocht *et al.*, 2020; Popuri *et al.*, 2021), we examined the role of glucose hypometabolism as a modifier of RAN translation. To model RAN translation *in vitro*, we used a human synapsin-driven lentiviral vector to ectopically express a $(GGGGCC)_{188}$ repeat expansion with a 3’ GFP tag (lacking an ATG start codon) in primary rodent neurons (

Figure 2A). Notably, we included the region of the C9orf72 gene located immediately upstream of the G_4C_2 repeat expansion – including exon 1a and a portion of intron 1 – which is thought to be required to initiate RAN translation from the sense strand (Tabet *et al*, 2018). Indeed, neurons transduced with this vector exhibit a clear GFP signal that accumulates into perinuclear and dendritic DPR inclusions (

Figure 2B), which are detectable by Western blot using both GFP- and DPR-specific antibodies (

Figure 2C). We then established an *in vitro* glucose hypometabolism paradigm by replacing a portion (up to 40%) of the glucose in the media with the glycolysis inhibitor 2-deoxyglucose (2DG), which caused downregulation of energy metabolism gene ontology (GO) pathways at the transcriptional level (**Figure EV2A**). We also found that 2DG treatment caused a sharp reduction of both extracellular acidification rate (ECAR) and oxygen consumption rate (OCR), as measured by the Seahorse extracellular flux assay (**Figure EV2B**), indicating functional impairment of energy metabolism. We then applied the 2DG treatment paradigm to neurons transduced with the RAN translation vector (

Figure 2D). Remarkably, we found that DPR formation was highly 2DG dose-dependent, with neurons treated with the highest 2DG concentration (10 mM) accumulating ~six times the number of DPR inclusions compared to non-treated cells (

Figure 2E), strongly suggesting that glucose hypometabolism increases DPR accumulation.

As a control, we performed the same experiment, but instead of using the RAN translation vector to drive DPR production, we used a separate ATG-driven vector encoding 50 codon-optimized GA repeats with a 3’ GFP tag (

Figure 2G). Importantly, the 2DG treatment did not affect the abundance of GA aggregates from this ATG-driven vector (

Figure 2H). This indicates that glucose hypometabolism selectively enhances RAN translation while having limited effects on ATG-driven translation. The findings suggest that RAN-translated DPR accumulation is due to increased production rather than decreased turnover since the GA aggregates made from both vectors are subject to the same molecular chaperones and degradative mechanisms. Finally, we observed no impact from the 2DG treatment on GFP mRNA levels (

Figure 2I), which indicates that the increase in aggregates is not due to changes in viral transduction or transcription efficiencies but reflects the upregulation of RAN translation.

Glucose hypometabolism causes DPR accumulation through the GCN2 arm of the ISR

To elucidate the mechanism through which glucose hypometabolism enhances the accumulation of DPRs, we first used RNA sequencing to identify the significant transcriptomic changes that occur in C9orf72 patient-derived induced pluripotent stem cell (iPSC) neurons upon 2DG treatment. Among the most highly upregulated pathways were those implicated in stress response, including “response to the endoplasmic reticulum (ER) stress,” “amino acid transport,” and “amino acid biosynthesis” (**Figure 3A**), which led us to consider cellular stress signaling as a potential mediator of increased RAN translation. In line with this, several studies have demonstrated that cellular stress can increase RAN translation by activating the ISR (Cheng *et al.*, 2018; Green *et al.*, 2017; Westergard *et al.*, 2019). The key on-switch for the ISR is phosphorylation of eIF2α, which is carried out by four different kinases – HRI, PKR, PERK, and GCN2 – each activated by different forms of stress (Pakos-Zebrucka *et al.*, 2016). A major outcome of eIF2α phosphorylation is ATF4 translational activation. ATF4 then translocates to the nucleus and activates transcription of numerous target genes (Pakos-Zebrucka *et al.*, 2016). Indeed, in our RNA-seq dataset, we observed upregulation of ATF4 and multiple known targets of ATF4 (**Fig. 3B**), indicating that 2DG treatment activates the ISR in C9orf72 patient-derived iPSC neurons. We also identified upregulation of ATF4 in spinal cord lysates from C9or72 patients (**Figure EV3A**), highlighting the relevance of ISR activation in C9-ALS/FTD.

We then confirmed that 2DG treatment activates the ISR in our primary rodent neuron model. Using immunofluorescent staining, we observed a 2DG dose-dependent increase in ATF4 nuclear intensity, specifically in MAP2-positive neurons (**Figure 3C**), which strongly correlated with DPR accumulation ($R^2 > 0.8$) (**Figure 4A**). This suggested that the increase in DPR accumulation was indeed mediated by ISR activation. To provide more evidence, we tested whether direct pharmacological inhibition of the ISR could also inhibit DPR accumulation caused by 2DG. Specifically, we blocked GCN2 because it is activated by nutrient deprivation stress (**Figure 4B**). Remarkably, we found that treatment of the neuronal cultures with A92 – a pharmacological inhibitor of GCN2 – completely prevented the increase in DPR accumulation caused by 2DG (**Figure 4C-D**) with an IC_{50} value of 1.6 μM (**Figure 4E**). Importantly, A92 had no deleterious effect on neuronal survival (**Figure EV3B**). Furthermore, ISRIB (a small molecule inhibitor of the ISR) could *also* block the increase in DPR formation caused by 2DG (**Figure EV3C**), further confirming the involvement of the ISR in augmenting DPR production. Lastly, we demonstrated that inhibition of GCN2 with A92 can block DPR formation caused by 2DG in human iPSC-derived neurons (**Figure EV3D**). Together, our data indicate that glucose hypometabolism enhances neuronal RAN translation through activation of the GCN2 arm of the ISR.

Glucose hypometabolism selectively impairs the survival of i^{3}Neurons from C9orf72 ALS patients through activation of the GCN2 kinase

Given the toxic profile of DPRs, we posit that glucose hypometabolism – by augmenting RAN translation – would cause a higher level of toxicity in neurons carrying the repeat expansion compared to healthy controls. We tested this hypothesis in hiPSC-derived neurons generated via doxycycline-inducible expression of pro-neural transcription factors (**Figure 5A**). This approach produces highly consistent and homogenous neuronal cultures (i^{3}Neurons), which express the full complement of neuronal markers and exhibit classic electrophysiological properties of neurons (Fernandopulle *et al*, 2018). We generated mature i^{3}Neurons from healthy controls and C9orf72 ALS patients, then removed glucose from the cell culture media (**Figure 5B**). This approach led to a time-dependent reduction in neuronal activity, which was rescued by the re-addition of glucose (**Figure EV4A**). Moreover, as with our 2DG treatment paradigm, we verified that complete glucose deprivation decreases the metabolic rate of the cells (**Figure EV4B**), causes ISR activation, and enhances DPR production (**Figure EV4C-F)**. We then tracked the survival of both control and C9 patient-derived i^{3}Neurons (with two iPS lines per genotype) cultured in glucose-deprived or normo-glucose media over six days and found that the C9 cells had markedly worse survival in glucose-deprived media compared to control cells, as well as compared to C9 cells cultured in normo-glucose (**Figure 5C-D**). Furthermore, we found that this C9-specific survival defect was ameliorated by culturing the cells with the GCN2 inhibitor A92 (**Figure 5E**), which may suggest that DPR production via GCN2 activation is potentially involved in the C9-specific vulnerability to glucose deprivation. However, the rescue we observed was incomplete, which may reflect the involvement of other pathogenic mechanisms caused by the repeat expansion besides DPR toxicity (for example, C9orf72 haploinsufficiency (Wang *et al*, 2021)).

Exacerbating energy imbalances increases DPR accumulation and causes motor dysfunction in the C9 BAC transgenic mouse

To corroborate our findings in an *in vivo* model and explore the potential downstream behavioral and phenotypical consequences of glucose hypometabolism in C9-ALS/ALS, we returned to the C9 BAC transgenic mouse. Despite exhibiting some basal level of dipeptide repeat pathology in several CNS regions, these mice do not manifest ALS-like motor dysfunction (O'Rourke *et al.*, 2015), which we hypothesized is due to *insufficient* production of DPRs. We further hypothesized that exacerbating metabolic dysfunction in these animals would cause significant stress to the CNS, increase DPR production, and cause the onset of a motor phenotype.

To target glucose metabolism in the CNS, we i.p. injected mice with 2DG (**Figure 6A**), which O’Connor and colleagues demonstrated to cause ISR activation in the murine CNS(O'Connor *et al*, 2008). We performed an initial experiment to confirm these results, and indeed, observed a 2DG dose-dependent increase in spinal cord mRNA levels of both CHOP and GADD34 (two downstream targets of the ISR) within 16 hours of 2DG injection (**Figure 6B**). However, we also observed acute toxicity in several animals treated with the highest dose (8 g/kg), and therefore we proceeded with further experiments using the intermediate dose (4 g/kg). We exposed animals to 4 g/kg 2DG weekly for six weeks. After the treatment course, we again employed LC-MS to confirm the presence of 2DG-6-P (the primary metabolite of 2DG) in the brain and assess the degree of metabolic alteration it caused. As expected, we detected 2DG-6-P accumulation in the brain of 2DG-injected animals (**Figure 6C**), as well as an increased concentration of fructose-1,6-bisphosphate and enrichment of metabolites involved pathways such as gluconeogenesis, transfer of acetyl groups into the mitochondria, the citric acid cycle, and several others (**Figure 6D, Figure EV5A, Table EV1**), which validates this approach as a method to introduce metabolic impairment in the CNS. Interestingly, using confocal scanning laser ophthalmoscopy (cSLO) imaging, we also observed evidence of retinal damage resulting from 2DG treatment. Specifically, compared to saline-treated, the 2DG-treated C9-BAC animals had a higher number of round hyperfluorescent foci (**Figure EV5B**), which are commonly associated with various pathological retinal conditions (Fragiotta *et al*, 2021). This further highlights the CNS effects of the 2DG injection paradigm.

But does 2DG-mediated metabolic impairment alter DPR production and/or motor function? Indeed, using both a dot blot immunoassay and a single molecule array (Simoa) assay, we observed higher GP levels in the spinal cord of 2DG-injected C9-BAC animals compared to those injected with saline (**Figure 6E, Figure EV5C**). Furthermore, we found that chronic 2DG treatment was accompanied by a worsening of motor performance, as indicated by a decreased latency to fall of 2DG-injected C9 animals on the inverted wire hang test (**Figure 6F**), which was independent of changes in body weight (**Figure EV5D**). Importantly, in wild-type animals, we *did not* detect a deficit in inverted wire hang performance (**Figure EV5E**), indicating that the deficit is specific to C9-BAC animals. Together, our data indicate that exacerbating metabolic imbalances and ISR activation *in vivo* enhances DPR production and causes a motor phenotype in a transgenic mouse model of C9-ALS/FTD.

PR contributes to neuronal glucose hypometabolism and ISR activation

We also wanted to determine whether RAN-translated DPRs could themselves contribute to neuronal glucose hypometabolism and ISR activation. We again employed synapsin-driven lentiviral vectors to drive DPR production in neurons, but for these experiments, we encoded the DPRs using a randomized codon strategy such that only one of the five possible DPRs would be expressed at any time and using an ATG start codon (**Figure 7A**). We also included a GFP tag downstream of the DPRs to visualize their cellular localization and used a GFP-only vector as a control. These vectors drive robust DPR/GFP expression with the expected cellular localization patterns. For example, the GFP fluorescence resulting from the PR vector mainly localizes to the nuclear and nucleolar regions of the cells (**Figure 7B**). We transduced cells with equivalent amounts of lentivirus for each construct (which we determined using qRT-PCR-based measurement of lentiviral titers; **Figure EV6A**) and found that each vector drove GFP/DPR expression with similar transduction efficiencies ranging from 85%-95% (**Figure EV6B-C**).

We then measured how these DPRs affect the neurons' ability to both take up and metabolize glucose. Interestingly, using a luminescence-based glucose uptake assay (which we first validated for use with neurons; **Figure EV6D**), we found that expression of PR (but not the other DPRs) caused a ~25% reduction in glucose uptake normalized to total protein, compared to the GFP control (**Figure 7C**). Furthermore, using the Seahorse flux assay, we found that expression of PR *also* caused a significant reduction in extracellular acidification rate (ECAR) normalized to total protein (**Figure 7D**), which is an indicator of the rate of glycolysis occurring in the cells. Therefore, our data indicate that the presence of PR in neurons is sufficient to impair glucose metabolism. We also detected a trend towards decreased oxygen consumption in PR-expressing neurons, indicating that impaired glucose metabolism caused by PR decreases the amount of pyruvate available for oxidative phosphorylation (**Figure EV6E**). As expected, we also found that PR-expressing neurons had a significantly higher nuclear ATF4 level (**Figure 7E**), which indicates that PR can *also* activate the ISR, potentially through its effect on glucose metabolism, although we cannot rule out the other mechanisms initiated by PR. Still, these data indicate that PR can independently contribute to neurons' energy imbalance and ISR activation in neurons.

Discussion

In this study, we identified a novel link between energy imbalance and disease pathogenesis in C9orf72-ALS/FTD, which uncovers several opportunities for therapeutic intervention. Specifically, we demonstrated that brain glucose hypometabolism – which is a consistently-observed phenomenon that occurs years before symptom onset in C9orf72 patients but also in other neurodegenerative diseases (Cunnane *et al.*, 2020; De Vocht *et al.*, 2020; Popuri *et al.*, 2021) – can act as a modifier of RAN translation and ultimately prime and exacerbate disease phenotypes, both in *in-vitro* and *in-vivo* models of disease. These findings are particularly important because they indicate that, by heightening the production of pathogenic DPRs, pre-symptomatic metabolic imbalances may play a central role in initiating or potentiating disease. This, in turn, highlights a critical window for therapeutic intervention to mitigate RAN translation and thereby delay disease onset or slow disease progression. Fortunately, many FDA-approved metabolic treatments already exist (Kinch *et al*, 2015) and could quite easily be repurposed to treat C9orf72 ALS/FTD patients. The compound taurursodiol – which, in combination with sodium phenylbutyrate, was recently approved by the FDA under the brand name Relyvrio for the treatment of ALS (Paganoni *et al*, 2020) – is known to enhance mitochondrial biogenesis (Soares *et al*, 2018) and may, in turn, enhance mitochondrial energy production, though its exact mechanism of action is unknown. Boosting energy production in the CNS could also be achieved through simple dietary manipulation, and indeed, both high-fat/high-calorie diet and acetyl-L-carnitine supplementation have already shown clear therapeutic potential in both pre-clinical studies and ALS clinical trials (Beghi *et al.*, 2013; Ludolph *et al.*, 2020). Another potentially powerful approach (though unexplored in C9orf72-ALS/FTD) is supplementation with the NAD^+ precursor nicotinamide mononucleotide (NMN), especially since we identified deficits in both NAD^+ and NMN in the brain of C9-BAC mice. Indeed, dietary supplementation with NMN has been shown to enhance NAD+ biosynthesis and, in turn, boost energy production (Xie *et al.*, 2020), and may therefore help to correct energy imbalances associated with the C9orf72 repeat expansion. Overall, our findings warrant additional clinical efforts to preserve bioenergetic homeostasis in C9orf72 ALS/FTD patients – including pre-symptomatic mutation carriers – to keep RAN translation at bay.

Our findings also highlight another potential therapeutic target for C9orf72-ALS/FTD: the integrated stress response (ISR). In support of this, we observed activation of the ISR both in neurons exposed to energy deprivation and in the spinal cord of C9orf72-ALS/FTD patients, highlighting the clinical relevance of ISR activation. But more importantly, we also found that pharmacological inhibition of GCN2 – which is one of the four kinases that controls ISR activation (Pakos-Zebrucka *et al.*, 2016) – completely blocked DPR accumulation caused by glucose hypometabolism, which suggests that GCN2 inhibition may serve as a viable therapeutic strategy to attenuate RAN translation caused by metabolic imbalances. Of note, ALS patients are subject to numerous other forms of stress in addition to that caused by energy imbalance (Masrori & Van Damme, 2020), and therefore, the potential contributions of the other three stress-sensing ISR kinases (i.e. PERK, PKR, and HRI) should also be considered. Indeed, several studies have identified roles for PERK and PKR in mediating RAN translation caused by oxidative stress and/or (GGGGCC) repeat-containing RNA, respectively (Cheng *et al.*, 2018; Green *et al.*, 2017; Westergard *et al.*, 2019; Zu *et al*, 2020). Moreover, perturbation to the mitochondria (also commonly seen in ALS) was recently found to activate HRI, the fourth ISR kinase (Guo *et al*, 2020). Therefore, rather than selective inhibition of individual ISR kinases, a comprehensive approach focusing on the direct reversal of eIF2α phosphorylation may prove to be more appropriate. A compound such as ISRIB would accomplish just that – and in fact, we also observed a rescue of RAN translation *in vitro* upon ISRIB treatment. However, this rescue was not complete, suggesting that other pathways known to respond to energy imbalance (for example, the mTOR pathway (Leprivier & Rotblat, 2020)) may also be involved. Additional studies are warranted to understand the full extent of the role of the ISR and other interconnected pathways as mediators of RAN translation and determine the most efficacious strategies to mitigate DPR production caused by energy imbalance and other forms of cellular stress.

We also identified significant brain energetic and metabolic alterations at baseline – with no pharmacological manipulation – in the frontal cortex of 6-month C9-BAC mice. Specifically, we observed a reduction in ATP levels (and ATP:ADP / ATP:AMP ratios) and alterations in glucose metabolic pathways such as glycolysis and gluconeogenesis. We also observed increased amino acid metabolism in C9-BAC animals, which may reflect a compensatory shift towards usage of amino acids as alternative substrates for oxidative metabolism. In line with these results, a recent study identified an increase in brain microvascular expression of GLUT1 – the sole glucose transporter present at the blood-brain barrier – also in an asymptomatic C9-BAC mouse model (Pan *et al*, 2022), which may reflect an attempt to compensate for altered brain glucose utilization. Based on these lines of evidence, the repeat expansion is sufficient to perturb brain energy homeostasis *in vivo*. The fact that this occurs in the absence of motor and cognitive behavioral phenotypes and overt neuropathology is somewhat surprising – however, these data mirror clinical findings showing that glucose hypometabolism can manifest years before disease onset (De Vocht *et al.*, 2020; Popuri *et al.*, 2021). C9orf72-related metabolic imbalances may accumulate without consequence for some time – potentially years in humans – before becoming disease-causative. Longitudinal metabolomic and transcriptomic studies would be useful to fully characterize the extent of metabolic imbalances caused by the G_4C_2 repeat expansion and may provide additional insight into how they accumulate or evolve. Potential non-cell-autonomous contributions to C9orf72-related energy imbalances would also be worth investigating, especially since C9orf72 patient-derived astrocytes exhibit metabolic inflexibility and may have an impaired capacity to provide metabolic support to neurons (Allen *et al*, 2019).

But *how* does the repeat expansion trigger metabolic imbalance *in vivo*? Since the C9-BAC mouse is a gain-of-function model and lacks neurodegeneration (which could confound metabolite measurements), the perturbations we identified in this study must be due to the gain-of-function of the G_4C_2 repeat expansion. A primary gain-of-function mechanism is DPR production through RAN translation, and in fact, we also found that the arginine-rich DPRs can disrupt glucose metabolism in cultured neurons. Furthermore, several other studies have found that GR localizes to the mitochondria and compromises mitochondrial function (Choi *et al*, 2019; Li *et al*, 2020; Lopez-Gonzalez *et al*, 2016). Therefore, we speculate that DPR production may contribute to the metabolic deficits we identified *in vivo*, although further studies will be required to confirm this. It is also worth noting that, in humans, in addition to causing RAN translation, the repeat expansion also causes haploinsufficiency of the endogenous C9orf72 protein, which potentially relevant to energy metabolism because the loss of C9orf72 was recently found to de-stabilize the electron transport chain (ETC) and in turn disrupt mitochondrial ATP production (Wang *et al.*, 2021). Therefore, future studies should aim to elucidate the potential synergistic roles of *both* gain-of-function mechanisms (i.e., DPR-mediated disruption of glycolysis) *and* loss-of-function mechanisms (i.e., de-stabilization of the ETC), as both would be expected to occur in human C9orf72-ALS/FTD carriers and contribute to energy imbalance.

Our data point towards a pathogenic feedforward loop in which stress from ALS-associated energy imbalances enhances RAN translation and accumulation of DPRs, exacerbating glucose hypometabolism and metabolic stress. In essence, brain energy metabolic decline, a feature of C9orf72-ALS/FTD but also observed in other neurodegenerative conditions, drives and is driven by neurodegeneration and neuronal impairment in a potentially destructive cycle. Therapeutically targeting this neurotoxic feedforward loop – either by correcting the energy imbalance or mitigating stress response activation – may be a powerful approach to mitigate neurodegeneration in C9orf72-ALS/FTD.

Acknowledgements

We thank Target ALS for providing the anti-GP antibody (cat # TALS 828.179) and Drs. M.E. Ward and S.J. Barmada for providing iPSC lines. We also thank the members of the Weinberg ALS Center for providing critical feedback throughout the development of this project. The following sources supported this work: National Institutes of Health F31-NS118838 (A.T.N.), R21-NS090912 (D.T.), RF1-AG057882 (D.T.), RF1-NS114128 (A.H.), and R01-NS109150 (P.P.); Muscular Dystrophy Association grant 628389 (D.T.); DoD grant W81XWH-21-1-0134 (M.E.C.); Family Strong for ALS, Farber Family Foundation, and the Greene Foundation (Weinberg ALS Center).

Author Contributions

A.T.N. and D.T. conceived the study, designed the experiments, interpreted the results, and wrote and revised the manuscript. A.T.N. performed all major experiments. D.T. supervised all experiments and provided the resources for the project. M.E.C. prepared primary neuron cultures. S.S.M. assisted in rodent dissections and western blotting. J.H. performed confocal scanning laser ophthalmoscopy. E.W. assisted in RNA sequencing analysis and interpretation. A.R.H., N.P., E.S., and P.P. provided conceptual input and critical feedback. G.M. and H.K. aided in metabolite profiling experimental design, analysis, and interpretation.

Disclosure and Competing Interests Statement

The authors declare no competing financial interests.

Materials and Methods

Targeted polar metabolite profiling

Metabolites from equal amounts of frontal cortex tissue were rapidly extracted in 80% ice-cold methanol. Extracted samples were vortexed twice, cleared by centrifugation at 14,000 x g for 20 minutes at 4°C, and stored at -80°C. The Weill Cornell Medicine Meyer Cancer Center Proteomics & Metabolomics Core Facility performed hydrophilic interaction liquid chromatography-mass spectrometry (LC-MS) for relative quantification of targeted polar metabolite profiles. Metabolites were measured on a Q Exactive Orbitrap mass spectrometer, coupled to a Vanquish UPLC system by an Ion Max ion source with a HESI II probe (Thermo Scientific). A Sequant ZIC-pHILIC column (2.1 mm i.d. × 150 mm, particle size of 5 µm, Millipore Sigma) was used for separation. The MS data were processed using XCalibur 4.1 (Thermo Scientific) to obtain the metabolite signal intensity for relative quantitation. Targeted identification was available for 205 metabolites based on an in-house library established using known chemical standards. Identification required exact mass (within 5ppm) and standard retention times. Relative metabolite abundance data were median-normalized and log-transformed, and differential abundance and pathway analyses were done with the free online tool MetaboAnalyst 5.0(Pang *et al*, 2021). Metabolite significance was determined with one-way ANOVA with posthoc t-tests, with the cutoff being a raw p-value < 0.05, and the pathway significance cutoff was an FDR < 0.05**.**

Lentiviral transfer vector construction and lentivirus preparation

For the RAN translation transfer vector, the 5' region of the *C9orf72* gene and the GFP tag were PCR-amplified from previously described plasmids(Wen *et al.*, 2014; Westergard *et al.*, 2019), then inserted into an AgeI-/EcoRI-linearized pLenti-hSyn backbone (Addgene #86641) by Gibson assembly. The $(GGGGCC)_{188}$ repeat expansion was generated using previously described protocols(Wen *et al.*, 2014), then introduced by classical restriction cloning. For each codon-optimized DPR_{50} transfer vector, the DPR-GFP sequences were PCR-amplified from previously described plasmids(Wen *et al.*, 2014), then inserted into an AgeI-/EcoRI-linearized pLenti-hSyn backbone (Addgene #86641) by Gibson assembly. The complete cloning strategies, primers (GeneWiz), and restriction enzymes (NEB) used are contained within the corresponding .dna files. All PCR products were amplified using a standard Q5 polymerase protocol (NEB) and purified with an agarose gel extraction kit (Thermo Scientific). Gibson assemblies and ligations were performed per the manufacturer's recommendations (Thermo Scientific). The sequences of all plasmids were verified by Sanger sequencing (GeneWiz).

Lentivirus was prepared by co-transfection of a confluent 15 cm plate of HEK 293-FT cells (Invitrogen) with 8 µg of transfer vector, 16 µg of packaging plasmid (psPAX2; Addgene #12260), and 4 µg of envelope plasmid (pMD2.G; Addgene #12259) with 112 µg PEI MAX (Polysciences, Inc.) as a transfection reagent. 48 hours later, the viral supernatant was harvested and filtered through a 0.45 µm PVDF syringe filter. Lentivirus was then concentrated using Lenti-X Concentrator (Takara Bio), reconstituted in PBS, and the resulting titers estimated using the Lenti-X qRT-PCR Titration Kit (Takara Bio), all following manufacturers' recommendations. Concentrated lentivirus was aliquoted and stored at -80°C.

Primary neuron preparation

Embryonic day 16 (E16) rat embryos were harvested, brains were dissected, and meninges removed. Cortical and midbrain regions were cut into small pieces and digested by exposure to 0.2% trypsin for 45 min at 37°C with gentle shaking, after which fetal bovine serum (FBS) was added to neutralize the digestion. The tissue was washed several times with HBSS and passed through a 70 µm strainer to create a single-cell suspension. The neurons were then plated in a neurobasal medium supplemented with B-27, penicillin-streptomycin, and L-glutamine on plates pre-coated with poly-D-lysine or a combination poly-D-lysine and laminin (for glass coverslips). Half media changes were performed twice weekly.

Induced pluripotent stem cell (iPSC) maintenance and differentiation

iPSC lines were obtained as generous gifts from the labs of Drs. Ward and Barmada and arrived in our lab. already genetically edited to contain doxycycline-inducible neuronal differentiation cassettes in the AAVS1 and CLYBL safe harbor loci (**Fig. 5A**). Standard hiPSC maintenance and differentiation protocols were adapted from a previous study(Fernandopulle *et al.*, 2018) and are described below.

General maintenance: The hiPSCs were grown as colonies on Matrigel-coated (Corning) 10 cm plates in Essential 8 (E8) medium (Fisher Scientific), which was changed daily. Spontaneous differentiation was identified under an Evos microscope and removed twice weekly by mechanical dissociation. Once reaching a confluency of ~80%, the colonies were removed from the plate by gentle scraping, then split 1:2 into new plates, with care taken to ensure the colonies remained intact. 10 µM rock inhibitor (Selleck Chemicals) was added to the media after splitting.

Differentiation into i^{3}Neurons: Differentiation was accomplished in two phases: 1) an induction phase from days post induction (DPI) 0-3, in which doxycycline (Sigma) was added to the media to facilitate gene induction and 2) a maturation phase (from DPI 3 and onwards), in which the cells were exposed to neurotrophic factors and allowed to differentiate to maturity. To initiate induction, hiPSCs were dissociated into a single-cell suspension with accutase (Fisher Scientific), re-plated onto matrigel-coated 10 cm plates (1-2 million cells per plate), and switched to doxycycline-containing “induction medium” consisting of DMEM/F12 with N2 supplement, glutamax, and NEAA (all Fisher Scientific). Induction media was replaced daily. For the maturation phase, the induced cells were re-plated onto poly-L-ornithine- (Sigma) and laminin- (Fisher Scientific) coated plates and switched to a “maturation medium” consisting of BrainPhys Neuronal Medium (StemCell Technologies) with B-27 supplement (Fisher Scientific), BDNF/NT3 (PeproTech), and laminin (Fisher Scientific). Half media changes with maturation media were performed twice weekly until the cells were utilized for experiments at DPI 21-27.

Neuronal transductions and treatments

At day *in vitro* (DIV) 8 (for primary neurons) and DPI21 (for i^{3}Neurons), lentiviral particles were diluted into fresh neuronal media at a concentration of $2x10^7$ lentiviral RNA copies/ml. The cells' media was then replaced with this virus-containing media – 72 hours later, the virus-containing media was replaced with fresh media.

For 2DG treatments, the cells were cultured with media containing 2DG (Cayman Chemical). Notably, the concentration of glucose (usually 25 mM) was adjusted accordingly to prevent osmotic stress (e.g., if media was prepared with 10 mM 2DG, the concentration of glucose was reduced to 15 mM), which was achieved by adding the desired concentrations of glucose/2DG to glucose-free Neurobasal (Fisher Scientific), then preparing the media as usual. Similarly, glucose-deprived media was prepared by replacing the glucose in the media with 25 mM mannitol (a metabolically inert compound; Sigma).

Immunofluorescence and confocal imaging analysis

Neurons grown on glass coverslips were washed once with PBS, then fixed with 4% PFA for 15 min. The cells were washed with PBS twice more, then permeabilized with 0.1% Triton-X for 15 min, blocked with 5% bovine serum albumin (BSA) for 45 min, then incubated overnight in a primary antibody (anti-ATF4, Cell Signaling Technologies D4B8, 1:500; anti-MAP2, Novus Biologicals NB200-213, 1:5000) diluted in 1% BSA. The following day, the cells were washed twice with PBS, then incubated for 45 min in the appropriate fluorophore-conjugated secondary antibody (Alexa Fluor, Invitrogen, 1:1000) in 1% BSA. After two additional washes with PBS and one wash with ultra-pure water, coverslips were mounted onto glass slides using Vectashield with DAPI (Vector Laboratories, H-1200-10) and sealed with clear nail polish.

Mounted coverslips were imaged in the appropriate fluorescent channels using Nikon A1R confocal microscope. Z-stack images (0.3 - 1.0 um step size) were taken across >5 randomly selected fields of view per experiment with either 20X or 60X objectives.

Maximum intensity projections were generated and analyzed using ImageJ software. DPR puncta were quantified using the ImageJ multi-point tool. ATF4 nuclear expression was measured using ImageJ by first creating regions of interest (ROIs) based on DAPI staining (for MAP2+ cells only) and then measuring ATF4 mean fluorescence intensity within each ROI. >30 randomly selected cells were analyzed per condition. GFP mean fluorescence intensity was measured similarly, but instead using MAP2 staining to define ROIs.

Time-lapse imaging and analysis

i^{3}Neurons were differentiated to DPI 21 on glass-bottom plates, then switched to either normo-glucose or glucose-deprived media containing the viability dye DRAQ7 (Abcam ab109202, 1:100). Immediately following the media change, the cells were imaged live using the Nikon Eclipse Ti microscope in both the brightfield and Cy5 channels across >5 randomly selected fields of view per condition. The same fields of view were imaged daily for the remainder of the experiment. Individual cells were tracked over time and marked dead when they accumulated DRAQ7 fluorescence. >100 cells were tracked per condition per experiment.

RNA analyses

Total RNA was extracted from either cultured neurons (>1.5x10^6) or mouse spinal cord tissue (10-20 mg) using the PureLink RNA Mini kit (Thermo Scientific) and treated with DNase I (NEB) according to the manufacturers' recommendations. RNA concentration and purity (OD 260/280 ratio) were assessed by Nanodrop.

Real-time PCR: 300 ng of total RNA was reverse transcribed using SuperScript IV Reverse Transcriptase (Thermo Scientific). The resulting cDNA was then used for real-time PCR (15 ng per reaction) with the following TaqMan assays: human CHOP, human GADD34, human

18S rRNA, mouse CHOP, mouse GADD34, mouse β-actin, rat β-actin, and GFP (all Thermo Scientific). The resulting C_t values were analyzed using the $2^{\Delta\Delta Ct}$ method and expressed as fold change.

RNA sequencing: Total RNA from two independent differentiations of two C9orf72 patient-derived i^3Neuron lines (n = 4) per condition were used. Samples with a minimum RNA integrity number (RIN) of 8.0 were used for library preparation, transcriptome sequencing, differential expression analysis, and gene ontology (GO) enrichment analysis, all of which were performed by Novogene Co., LTD (Beijing, China). An adjusted p-value < 0.05 was set as the threshold for significance.

Glucose uptake assays

Primary rat neurons were plated in standard plastic 96-well plates at a density of 40,000 cells/well, then transduced with codon-optimized lentiviruses as described in the previous section. Four days after transduction, the Glucose Uptake-Glo assay (Promega) was performed according to the manufacturer's instructions. The reactions were then transferred to opaque white 96-well plates, and the luminescence was measured using standard luminometer settings on the Cytation 5 plate reader (BioTek). An aliquot of Glucose Uptake Glo assay lysates was analyzed for total protein content using the Pierce 660 nm protein assay according to the manufacturer's instructions and with Ionic Detergent Compatibility Reagent (Thermo Scientific). Luminescence values were then normalized to total protein.

Seahorse extracellular flux assays

Primary rat neurons or human i^3Neurons were plated on Seahorse XFp plates (Agilent) at a density of 40,000 cells/well, then either treated with 2DG or transduced with codon-optimized lentiviruses as described in previous sections. 48 hours after 2DG treatment or 4 days after transduction, the Seahorse Extracellular Flux assay was performed using the Seahorse XF Mini instrument (Agilent) according to the manufacturer's instructions. During the assay, the cells were treated sequentially with each of the following mitochondrial toxins: oligomycin (1.5 µg/ml), FCCP (3 µM), and antimycin (1 µM) (all Cayman Chemical). Immediately after the assay, the cells were lysed with RIPA buffer with protease inhibitor (Thermo Scientific). The lysates were analyzed for total protein content using the Pierce BCA protein assay (Thermo Scientific). Extracellular acidification rate (ECAR) and oxygen consumption rate (OCR) values were then normalized to total protein.

Lysate preparation for immunoassays

Human tissues: 100 mg of fresh-frozen spinal cord tissue was submerged in 1% SDS buffer with protease inhibitor (Fisher Scientific) and homogenized with a Dounce homogenizer. The resulting lysates were centrifuged at 3,000 rcf for 20 min at 4°C.

Mouse tissues (for GP immunoassays): 15-25 mg of fresh-frozen spinal cord tissue was submerged in 8M urea / 1% Triton-X buffer with protease inhibitor, triturated with a pipette, and homogenized with a handheld homogenizer. Lysates were then sonicated at 12°C with a tip sonicator 3-4x for 10 seconds each (until clear) and centrifuged at 18,000 rcf for 5 min at room temperature.

Cultured cells: 1-2 million cells in 6-well culture plates were washed with ice-cold PBS, submerged with 150 µl RIPA buffer with protease inhibitor and placed on an orbital shaker at 4°C for 15 min. Lysates were transferred to fresh tubes, sonicated with the Bioruptor Pico-Diagenode, and centrifuged at 18,000 rcf for 5 min at 4°C.

For all lysates, the clarified supernatant was moved to fresh tubes and Pierce BCA protein assay (Thermo Scientific) was used to measure the protein content of each sample. If used for Western blotting, the samples were mixed 1:1 with 2X Laemmli sample buffer (Bio-Rad) with 5% β-mercaptoethanol (Sigma) and heated to 95 C for 5 min. Samples (with or without sample buffer) were then aliquoted and stored at -80°C.

Immunoblotting

For Western blots, 10-30 µg of protein extracts were run at 100V for 1 hr on 10% pre-cast SDS-PAGE gels (Bio-Rad), then electro-transferred to 0.2 µm nitrocellulose membranes using the Trans-Blot Turbo Transfer system (Bio-Rad). For dot bots, 2-3 µg of protein extracts were blotted directly onto 0.2 µm nitrocellulose membranes and allowed to air dry for 30 min. Membranes were then blocked for 1 hr with 5% milk, incubated with primary antibody (anti-C9orf72/C9RANT (poly-GA), Millipore MABN889, 1:500; anti-GFP, Proteintech 50430-2-AP, 1:2000; anti-ATF4, Cell Signaling Technologies D4B8, 1:1000; anti-Histone H3, Cell Signaling Technologies D1H2) diluted in 5% BSA (either overnight at 4°C or 30 min at room temperature), washed 3x with TBS-T, incubated with HRP-conjugated secondary antibody diluted in 5% milk for 45 min at room temperature, and washed again 3x with TBS-T. Membranes were developed with SuperSignal West Femto Maximum Sensitivity substrate (Thermo Scientific). Images were acquired using the ChemiDoc XRS+ system (Bio-Rad).

Single-molecule array (Simoa) immunoassays

A custom "Homebrew" Simoa GP assay was performed using the SR-X Simoa platform (Quanterix). Mouse spinal cord lysates (in 8M urea buffer) were adjusted to 1 mg/ml protein and 4M urea; serial dilutions of recombinant GP_8 (custom synthesized by Vivitide) were also prepared in 4M urea buffer. All samples were then diluted 1:10 with Simoa Lysate Diluent C (Quanterix). Then, on a 96-well Simoa assay plate, samples were mixed with 1) anti-GP monoclonal antibody (Developmental Hybridoma Studies Bank; TALS 828.179)-coated paramagnetic capture beads, and 2) biotinylated anti-GP polyclonal detector antibody (Proteintech 24494-1-AP). After washing steps, a conjugate of streptavidin-β-galactosidase (SβG) was added to label the captured GP. After additional washing, resorufin β-D-galactopyranoside (RGP, i.e. the substrate for SBG) was added, and the labeled beads were transferred to the Simoa array. Fluorescent signal was captured and quantified by the SR-X instrument as average enzymes per bead (AEB), and then the GP concentration of each unknown lysate was interpolated from the GP standard curve.

Animals, drug treatments, and phenotypic analyses

All procedures involving mice were approved by the Institutional Animal Care and Use Committee (IACUC) at Thomas Jefferson University. All animals were housed in standard cages and provided food and water *ad libitum* in a temperature-, light-, and humidity-controlled animal facility. 6-month-old Tg(C9orf72_i3)112Lutzy (Jackson Laboratory) and wild-type littermate mice were administered i.p. injections of saline (vehicle) or 2 g/kg 2DG (Cayman Chemical). For acute studies, animals were administered either a single dose (2 g/kg 2DG), or higher doses (4-8 g/kg 2DG) which were achieved by repeated injections with 2 g/kg 2DG each spaced out by 1-2 hours. For chronic studies, animals were injected twice weekly with 2 g/kg 2DG for six weeks. For all studies, animals were euthanized by CO_2 inhalation 16 hours following the final injection and transcardially perfused with ice-cold PBS. Whole brains and spinal cords were then excised, flash frozen in liquid N_2, and stored at –80°C for biochemical analysis.

For inverted wire hang motor assessments, animals were suspended upside-down from a wire mesh and their latency to fall (capped at 180 seconds) was recorded. Each animal was given 3-4 independent trials with >10 minutes of rest between each trial. Baseline assessments were acquired several days before the first 2DG injection; subsequent assessments were acquired weekly and on a different day than the 2DG injections. The average of the 3 trials for each animal at each time-point was used for analysis. All test sessions were performed in the light cycle phase (10 am – 5 pm).

For confocal scanning laser ophthalmoscopy (cSLO) imaging, mice were anesthetized with ketamine (100 mg/kg) and xylazine (10 mg/kg) and eyes were anesthetized with 0.5% proparacaine HCl ophthalmic solution (NDC: 17478-263-12, Akorn). Pupils were dilated with 1% tropicamide eye drops (NDC: 17478-102-12, Akorn). Ocular eye shields and Systane Ultra Lubricant Eye Drops (Alcon Laboratories) were used to keep eyes hydrated. cSLO images were obtained using a Spectralis HRA+OCT (Heidelberg Engineering). Mice were positioned with the optic nerve in the center of the image using a 55° field of view (FOV) lens and imaged with two different modes, infrared (IR) and blue autofluorescence (BAF). All images were acquired with the auto-normalization activated, which provided the best contrast.

Statistical analyses

All statistical analyses were performed using GraphPad Prism 9.0 – these include Kaplan-Meier survival assessment with log-rank testing (to compare survival curves), student's two-tailed t-test (to compare the means of two groups), two-tailed t-test with Welch's correction (to compare the means of two groups with unequal variances or sample sizes), one-way analysis of variance (ANOVA) with Dunnett's multiple comparisons test or two-way ANOVA (to compare the means of more than two groups). A minimum of 30 individual cells were analyzed per condition for single-cell analyses. Data are reported as mean ± SEM. p-value < 0.05 was considered statistically significant.

Data Availability

The RNA-seq and metabolomics data produced in this study are in the process of being uploaded to Gene Expression Omnibus (https://www.ncbi.nlm.nih.gov/geo/) and Metabolomics orkbench (https://www.metabolomicsworkbench.org/), respectively. The sequences for all DNA plasmids used in this study are uploaded to GenBank (https://www.ncbi.nlm.nih.gov/genbank/) with the following accession numbers:

BankIt2694892 pLV_hSyn_GA188_EGFP	OQ828708
BankIt2694894 pLV_hSyn_GFP	OQ828709

BankIt2694876 pLV_hSyn_GA50_GFP	OQ828707
BankIt2694895 pLV_hSyn_GR50_GFP	OQ828710
BankIt2694896 pLV_hSyn_PA50_GFP	OQ828711
BankIt2694899 pLV_hSyn_PR50_GFP	OQ828712

Figure Legends

Figure 1 – The C9orf72-linked G_4C_2 repeat expansion disrupts brain energy balance.

A Schematic depicting brain metabolite profiling experimental setup.

B Principal component analysis (PCA) of the complete metabolomics panel.

C Liquid chromatography mass spectrometry (LC-MS) measurement of relative ATP concentrations, ATP:ADP ratios, and ATP:AMP ratios in C9-BAC animals versus WT animals.

D Enrichment analysis of metabolite sets in C9-BAC animals versus WT animals. Enrichment ratio represents the number of metabolites within each metabolite set that are either increased (in blue) or decreased (in red) in the frontal cortex of C9-BAC versus WT animals.

E Schematic of glycolysis pathway, with significantly altered glycolytic intermediates highlighted in blue text (decreased in C9-BAC animals) or red text (increased in C9-BAC animals). LC-MS measurement of relative concentrations of glucose-6-phosphate (G6P), glyceraldehyde-3-phosphate (GADP), and phosphoenolpyruvate (PEP) in C9-BAC versus WT animals.

F LC-MS measurement of nicotinamide adenine dinucleotide (NAD^+) and nicotinamide mononucleotide (NMN) concentrations in C9-BAC versus WT animals. All individual metabolite data are shown as median-normalized and log-transformed values (abbreviated as "Normalized conc.").

Data Information | For all data, n = 7 C9orf72 BAC+ (C9-BAC) and 6 littermate control wild type (WT) animals. For all box and whisker plots, box edges denote upper and lower quartiles, horizontal lines within each box denote median values, whiskers denote maximum and minimum values, and shaded circles denote individual values for each animal. Student's two-tailed t-test, * $p < 0.05$; ** $p < 0.01$; **** $p < 0.0001$.

Figure 2 – Glucose hypometabolism triggers accumulation of DPRs.

A Schematic of lentiviral RAN translation vector used for the experiments, containing a $(G_4C_2)_{188}$ repeat expansion with the 5' flanking region of the C9orf72 gene (including exon 1a and intron 1) and a downstream GFP tag lacking an ATG start codon in frame with GA. The entire construct was driven by the human synapsin (hSyn) promoter.

B Representative images depicting cellular localization patterns of RAN-translated GA-GFP aggregates.

C Western blot analysis of GA-GFP levels in primary neurons using anti-GA antibody (RRID: AB_2728663) (NT = non-transduced; GFP = transduced with a GFP lentiviral vector (negative control); G_4C_2-GFP = transduced with RAN translation vector).

D Schematic of experimental timeline from day *in vitro* (DIV) 0 to 10.

E Fluorescent confocal imaging and quantification of DPR aggregate formation in primary neurons transduced with RAN translation vector, then incubated with either normo-glucose media (25 mM glucose + 0 mM 2DG) or media containing increasing concentrations of 2DG (n = 4).

F qRT-PCR analysis of GFP mRNA levels in primary neurons transduced with either the RAN translation reporter vector, then incubated with either normo-glucose media or 10 mM 2DG-containing media (n = 4).

G Schematic of lentiviral ATG translation vector used for the experiments, containing a 50 GA repeats encoded with alternative codons and a downstream GFP tag.

H Fluorescent imaging and quantification of DPR aggregate formation in primary neurons transduced with ATG translation vector, then incubated with either normo-glucose media or 10 mM 2DG-containing media (n = 3).

I qRT-PCR analysis of GFP mRNA levels in primary neurons transduced with the ATG translation vector, then incubated with either normo-glucose media or 10 mM 2DG-containing media (n = 3).

Data Information | For **E**, one way ANOVA with Dunnett's test for multiple comparisons. For **F-I**, student's two-tailed t-test. All data are presented as mean ± standard error of the mean (SEM). ** $p < 0.01$, *** $p < 0.001$, **** $p < 0.0001$, n.s. $p > 0$

Figure 3 – Glucose hypometabolism activates the ISR in cultured neurons.

A, B RNA sequencing assessment of select transcriptomic changes in C9orf72 patient-derived i^3Neurons (n = 2 individual i^3Neuron lines with 2 separate differentiations per line) incubated in media containing 10 mM 2DG for 48 hours versus those maintained in normal media, including significantly upregulated gene ontology (GO) pathways (**A**) and significantly upregulated individual integrated stress response (ISR) target transcripts (**B**; all $p_{adj} < 0.05$).

C Immunofluorescence-based measurement and quantification of nuclear ATF4 expression level in MAP2-positive primary neurons incubated in media containing 0, 2.5, 5.0, or 10 mM 2DG for 48 hours (n = 4).

Data Information | For **A**, the values adjacent to each bar represent the number of altered genes in each GO pathway. For **B**, bars represent median values, and individual dots represent individual replicates. For **C**, one-way ANOVA with Dunnett's test for multiple comparisons. Data are presented as mean ± SEM. * $p < 0.05$, ** $p < 0.01$, **** $p < 0.0001$.

Figure 4 – DPR accumulation caused by glucose hypometabolism correlates with ISR activation and is blocked by inhibition of the GCN2 kinase.

A Correlation between number of GA-GFP aggregates per field of view (from **Fig. 2E**) and nuclear ATF4 expression level (from **Fig. 3C**) in primary neurons incubated with either normo-glucose or various concentrations of 2DG. Best-fit line and R^2 value represent linear regression analysis.

B Schematic depicting the proposed mechanism through which nutrient deprivation increases RAN translation. A92 was used as a pharmacological inhibitor of GCN2 kinase activity.

C, D Fluorescent confocal imaging and quantification of DPR formation in primary neurons transduced with RAN translation vector, then incubated with either normo-glucose media, 10 mM 2DG-containing media, or 10 mM 2DG-containing media with 5.0 μM A92, all in the presence of 0.1% DMSO (n = 4).

E Quantification of DPR aggregate formation in primary neurons transduced with RAN translation vector, then treated with A92 concentrations ranging from 0.1 μM to 7.5 μM, all in the presence of 10 mM 2DG and 0.1% DMSO (n = 4). Best-fit line and IC_{50} value were derived from non-linear regression analysis.

Data Information | For **D**, one-way ANOVA with Dunnett's test for multiple comparisons. All data are presented as mean ± SEM. **** $p < 0.0001$.

Figure 5 – Glucose deprivation is selectively toxic to C9orf72 patient-derived i^{3}Neurons.

A Schematic of the doxycycline-inducible neuronal differentiation cassette used to drive rapid differentiation of human induced pluripotent stem cells (hiPSCs) into i^{3}Neurons from days post-induction (DPI) 0 to 27.

B Timeline of differentiation into i^{3}Neurons and subsequent glucose deprivation.

C Live-cell longitudinal imaging of healthy control- or C9orf72 patient-derived i^{3}Neurons cultured with glucose-deprived media over 6 days using DRAQ7 as a dead cell indicator.

D Kaplan-Meier survival analysis of i^{3}Neurons derived from either C9orf72 patients or healthy controls and maintained in glucose-deprived media (n = 2 i^{3}Neuron lines per genotype with 3 independent differentiations per line).

E Kaplan-Meier survival analysis of C9orf72 patient-derived i^{3}Neurons maintained in either normo-glucose or glucose-deprived media and treated with either 2.5 μM A92 with 0.1% DMSO or 0.1% DMSO only as vehicle control (n = 2 i^{3}Neuron lines per treatment with 3 independent differentiations per line).

Data Information | For **D-E**, Dotted traces denote i^{3}Neuron lines with only Ngn2 integrated into the safe harbor locus (from Ward laboratory), while solid traces correspond to i^{3}Neuron lines with both Ngn1 and Ngn2 integrated into the safe harbor locus (from Barmada laboratory). Kaplan-Meier log-rank survival test. * $p < 0.05$, **** $p < 0.0001$.

Figure 6 – 2DG treatment exacerbates metabolic stress and drives disease-related phenotypes in C9orf72 BAC transgenic mice.

A Schematic of experimental setup: C9-BAC animals were treated with either 2-deoxyglucose (2DG) or saline (vehicle control) by i.p. injection.

B RT-qPCR measurement of spinal cord mRNA levels of two ISR transcriptional targets (CHOP and GADD34) in C9-BAC animals acutely treated with various doses of 2DG or saline (n = 3-4 animals per condition).

C, D LC-MS measurement of 2DG-6-P levels (**C**) and significantly altered metabolites (**D**) in the frontal cortex of C9-BAC mice following chronic weekly exposure to 4 g/kg 2DG versus saline (n = 7 animals per condition). Dark shaded lines indicate significance cut-offs ($-\log_{10}(p) > 1.3$ and $\log_2(FC) > |1|$).

E Dot blot assessment and corresponding quantification of 8M urea-soluble GP levels relative to total protein levels in the spinal cord C9-BAC animals treated with either saline (n = 3 animals) or 2DG (n = 6 animals). Bovine serum albumin (BSA) and spinal cord lysate from a wild-type animal were used as controls.

F Longitudinal assessment of inverted wire hang performance of C9-BAC animals chronically exposed to 4 g/kg 2DG or saline (n = 7 animals per condition).

Data Information | For **B**, one-way ANOVA with Dunnett's test for multiple comparisons. For **C-D**, student's two-tailed t-test. For **E**, two-tailed t-test with Welch's correction. For **F**, two-way ANOVA. All data are presented as mean ± SEM. * $p < 0.05$, *** $p < 0.001$, **** $p < 0.0001$.

Figure 7 – Arginine-rich DPRs contribute to glucose hypometabolic stress.

A Schematic of lentiviral DPR vectors and GFP-only (control) vector.

B Representative images depicting cellular localization patterns of GFP-tagged DPRs in primary neurons transduced with lentiviral vectors. **c** Luminescence-based measurement of glucose uptake (normalized to total protein) in primary neurons transduced with each of the DPR vectors or the GFP-only control vector (n = 4).

D Seahorse extracellular flux assay measurement of extracellular acidification rate (ECAR; normalized to total protein) of primary neurons transduced with either the PR vector or GFP-only control vector (n = 3).

E Immunofluorescence-based measurement and quantification of nuclear ATF4 expression level in MAP2-positive primary neurons transduced with either the PR vector or GFP-only control vector (n = 4).

Data Information | For **C**, one-way ANOVA with Dunnett's test for multiple comparisons. For **D**, multiple student's two-tailed t-tests. For **E**, student's two-tailed t-test. All data are presented as mean ± SEM. * $p < 0.05$, ** $p < 0.01$, **** $p < 0.0001$.

Figure EV1.

A Schematic depicting the bacterial artificial chromosome (BAC) transgene used to drive expression of the entire human *C9orf72* gene with a $(GGGGCC)_{100\text{-}1,000}$ repeat expansion in intron 1 (C9-BAC). Adapted from O'Rourke et al[33].

B LC-MS measurement of relative glucose concentrations in the frontal cortex of C9-BAC versus WT animals.

C Schematic depicting the tricarboxylic acid (TCA) cycle pathway with all metabolic intermediates. LC-MS measurement of relative α-ketoglutarate concentrations in the frontal cortex of C9-BAC animals versus WT animals.

D LC-MS measurement of the relative concentrations of four amino acids (isoleucine, cysteine, lysine, and ornithine) in the frontal cortex of C9-BAC vs. WT animals.

E LC-MS measurement of relative NADP+, NADH, and NADPH concentrations in the frontal cortex of C9-BAC vs WT.

Data Information | All individual metabolite data are shown as median-normalized and log-transformed values (abbreviated as "Normalized conc."). For box and whisker plots, box edges denote upper and lower quartiles, horizontal lines within each box denote median values, whiskers denote maximum and minimum values, and shaded circles denote individual values for each animal. Student's two-tailed t-test, * $p < 0.05$, ** $p < 0.01$, **** $p < 0.0001$.

Figure EV2.

A RNA sequencing measurement of select downregulated gene ontology (GO) pathways in C9orf72 patient-derived i^3Neurons incubated with 10 mM 2DG-containing media versus normo-glucose media for 48 hours ($n = 2$ individual i^3Neuron lines with 2 separate differentiations per line).

B Seahorse extracellular flux assay-based measurement of extracellular acidification rate (ECAR) normalized to total protein and oxygen consumption rate (OCR) normalized to total protein in primary neurons incubated with either normo-glucose media or 10 mM 2DG-containing media for 48 hours. Cells were sequentially treated with 1.5 µg/ml oligomycin (o.), 3 µM FCCP (f.), and 1 µM antimycin (a.) during the assay ($n = 1$).

Data Information | For **A**, the values adjacent to each bar represent the number of altered genes in each GO pathway. For **B**, data are presented as mean ± SEM of assay technical replicates.

Figure EV3.

A Western blot analysis and quantification of ATF4 expression level relative to histone H3 expression level (as a loading control) in lumbar spinal cord tissue homogenates from either healthy control subjects or C9orf72-ALS patients ($n = 3$ subjects per genotype).

B Live-cell imaging of human i^3Neurons treated with either 0.1% DMSO or 5.0 uM A92 and 0.1% DMSO for 48 hours, with corresponding quantification of survival proportions. DRAQ7 was used as a fluorescent dead cell indicator ($n = 2$ i^3Neuron lines with 2 independent differentiations per line).

C Fluorescent confocal imaging and quantification of DPR aggregate formation in primary neurons transduced with RAN translation vector, then incubated with either normo-glucose media, 10 mM 2DG-containing media, or 10 mM 2DG-containing media with 0.5 uM or 5 uM ISRIB (all in the presence of 0.1% DMSO; $n = 4$).

D Fluorescent confocal imaging and quantification of DPR formation in human i^3Neurons transduced with RAN translation vector, then incubated with either normo-glucose media, 10 mM 2DG-containing media, or 10 mM 2DG-containing media with 2.5 uM A92 (all in the presence of 0.1% DMSO; $n = 1$).

Data Information | For **A-B**, student's two-tailed t-test. For **C**, one-way ANOVA with Dunnett's test for multiple comparisons. All data are presented as mean ± SEM. * $p < 0.05$, ** $p < 0.01$, *** $p < 0.001$, **** $p < 0.0001$.

Figure EV4.

A Longitudinal microelectrode array (MEA)-based measurement of spontaneous neuronal activity of i^3Neurons (healthy control line) incubated in either normo-glucose or glucose-deprived media over a 48-hour period ($n = 3$). Glucose deprivation was initiated at time = 0 h.

B Seahorse extracellular flux assay-based measurement of extracellular acidification rate (ECAR) normalized to total protein and oxygen consumption rate (OCR) normalized to total protein of primary neurons immediately following incubation with either normo-glucose media or glucose-deprived media for 48 hours ($n = 1$). Cells were sequentially treated 1.5 µg/ml oligomycin (o.) and 3 µM FCCP (f.) during the assay.

C Immunofluorescence-based measurement and quantification of nuclear ATF4 expression level in MAP2-positive primary neurons immediately following incubation with either normo-glucose media or glucose-deprived media for 48 hours ($n = 4$).

D RNA sequencing analysis of select individual ISR target transcripts (all $p_{adj} < 0.05$) in i^3Neurons immediately following exposure to either normo-glucose or glucose-deprived media for 48 hours ($n = 2$ i^3Neuron lines with 2 differentiations per line).

E Representative images of i^3Neurons transduced with RAN translation vector and then cultured in either normo-glucose or glucose-deprived media for 48 hours, with corresponding quantification of GA-GFP fluorescence intensity ($n = 3$).

F qRT-PCR measurement of mRNA levels of two ISR transcriptional targets (CHOP and GADD34) in i^3Neurons immediately following incubation with either normo-glucose or glucose-deprived media for either 24, 48, or 72 hours ($n = 1$).

Data Information | For **A**, multiple student's two-tailed t-tests. For **C-E**, student's two-tailed t-test. All data (except **D** and **F**) are presented as mean ± SEM. * $p < 0.05$, ** $p < 0.01$, *** $p < 0.001$.

Figure EV5.

A Enrichment analysis of significantly altered metabolite sets in the frontal cortex of C9-BAC animals immediately following chronic exposure to either 4 g/kg/week 2DG or saline (n = 7 animals per condition). Enrichment ratio represents the number of metabolites within each metabolite set that are either increased (on the left) or decreased (on the right).

B Optical coherence tomography (OCT) retinal imaging of C9-BAC animals immediately following chronic exposure to either 4 g/kg/week 2DG or saline. Yellow arrows indicate hyperreflective foci (n = 2-3 animals per condition).

C Single molecule array (Simoa) measurement of 8M urea-soluble GP levels relative to total protein levels in the spinal cord of saline-treated wild type animals (n = 3), saline-treated C9-BAC animals (n = 4), or 2DG-treated C9-BAC animals (n = 6).

D Longitudinal measurement of bodyweight during chronic exposure of C9-BAC animals to 4 g/kg/week 2DG or saline (n = 7 animals per condition).

E Longitudinal assessment of inverted wire hang performance of wild-type littermate control animals chronically exposed to 4 g/kg/week 2DG (n = 2 animals) or saline (n = 3 animals).

Data Information | For **C**, two-tailed t-test with Welch's correction. For **D-E**, two-way ANOVA. All data (except **A**) are presented as mean ± SEM. * $p < 0.05$, n.s. $p > 0.05$.

Figure EV6.

A qRT-PCR measurement of DPR and GFP-only vector lentiviral titers (n = 1).

B Representative images of primary neurons transduced with DPR or GFP-only lentiviral vectors, then stained for MAP2.

C Quantification of the percentage of MAP2-positive cells also positive for GFP from (**B**).

D Validation of luminescent assay (time- and temperature dependence) for measurement of glucose uptake in primary neurons (n = 1).

E Seahorse extracellular flux assay measurement of oxygen consumption rate (OCR normalized to total protein) of primary neurons transduced with either the PR or GFP-only vector (n = 3). Cells were sequentially treated with 1.5 μg/ml oligomycin (o.), 3 μM FCCP (f.), and 1 μM antimycin (a.) during the assay.

Data Information | All data (except **A**) are presented as mean ± SEM. For **C**, one-way ANOVA with Dunnett's multiple comparisons tests. For **E**, multiple student's two-tailed t-test. n.s. $p > 0.05$.

References

Allen SP, Hall B, Woof R, Francis L, Gatto N, Shaw AC, Myszczynska M, Hemingway J, Coldicott I, Willcock A *et al* (2019) C9orf72 expansion within astrocytes reduces metabolic flexibility in amyotrophic lateral sclerosis. *Brain* 142: 3771-3790

Ash Peter EA, Bieniek Kevin F, Gendron Tania F, Caulfield T, Lin W-L, DeJesus-Hernandez M, van Blitterswijk Marka M, Jansen-West K, Paul Joseph W, Rademakers R *et al* (2013) Unconventional Translation of C9ORF72 GGGGCC Expansion Generates Insoluble Polypeptides Specific to c9FTD/ALS. *Neuron* 77: 639-646

Beghi E, Pupillo E, Bonito V, Buzzi P, Caponnetto C, Chio A, Corbo M, Giannini F, Inghilleri M, Bella VL *et al* (2013) Randomized double-blind placebo-controlled trial of acetyl-L-carnitine for ALS. *Amyotroph Lateral Scler Frontotemporal Degener* 14: 397-405

Cheng W, Wang S, Mestre AA, Fu C, Makarem A, Xian F, Hayes LR, Lopez-Gonzalez R, Drenner K, Jiang J *et al* (2018) C9ORF72 GGGGCC repeat-associated non-AUG translation is upregulated by stress through eIF2alpha phosphorylation. *Nat Commun* 9: 51

Chighine A, Locci E, Nioi M, d'Aloja E (2021) Looking for Post-Mortem Metabolomic Standardization: Waiting for Godot-The Importance of Post-Mortem Interval in Forensic Metabolomics. *Chem Res Toxicol* 34: 1946-1947

Choi SY, Lopez-Gonzalez R, Krishnan G, Phillips HL, Li AN, Seeley WW, Yao WD, Almeida S, Gao FB (2019) C9ORF72-ALS/FTD-associated poly(GR) binds Atp5a1 and compromises mitochondrial function in vivo. *Nat Neurosci* 22: 851-862

Cunnane SC, Trushina E, Morland C, Prigione A, Casadesus G, Andrews ZB, Beal MF, Bergersen LH, Brinton RD, de la Monte S *et al* (2020) Brain energy rescue: an emerging therapeutic concept for neurodegenerative disorders of ageing. *Nat Rev Drug Discov* 19: 609-633

De Vocht J, Blommaert J, Devrome M, Radwan A, Van Weehaeghe D, De Schaepdryver M, Ceccarini J, Rezaei A, Schramm G, van Aalst J *et al* (2020) Use of Multimodal Imaging and Clinical Biomarkers in Presymptomatic Carriers of C9orf72 Repeat Expansion. *JAMA Neurol* 77: 1008-1017

DeJesus-Hernandez M, Mackenzie IR, Boeve BF, Boxer AL, Baker M, Rutherford NJ, Nicholson AM, Finch NA, Flynn H, Adamson J *et al* (2011) Expanded GGGGCC hexanucleotide repeat in noncoding region of C9ORF72 causes chromosome 9p-linked FTD and ALS. *Neuron* 72: 245-256

Dienel GA (2019) Brain Glucose Metabolism: Integration of Energetics with Function. *Physiol Rev* 99: 949-1045

Fayemendy P, Marin B, Labrunie A, Boirie Y, Walrand S, Achamrah N, Coeffier M, Preux PM, Lautrette G, Desport JC *et al* (2021) Hypermetabolism is a reality in amyotrophic lateral sclerosis compared to healthy subjects. *J Neurol Sci* 420: 117257

Fernandopulle MS, Prestil P, Grunseich C, Wang C, Gan L, Ward ME (2018) Transcription Factor-Mediated Differentiation of Human iPSCs into Neurons. *Curr Protoc Cell Biol* 79

Fragiotta S, Abdolrahimzadeh S, Dolz-Marco R, Sakurada Y, Gal-Or O, Scuderi G (2021) Significance of Hyperreflective Foci as an Optical Coherence Tomography Biomarker in Retinal Diseases: Characterization and Clinical Implications. *J Ophthalmol* 2021: 6096017

Green KM, Glineburg MR, Kearse MG, Flores BN, Linsalata AE, Fedak SJ, Goldstrohm AC, Barmada SJ, Todd PK (2017) RAN translation at C9orf72-associated repeat expansions is selectively enhanced by the integrated stress response. *Nat Commun* 8: 2005

Guo X, Aviles G, Liu Y, Tian R, Unger BA, Lin YT, Wiita AP, Xu K, Correia MA, Kampmann M (2020) Mitochondrial stress is relayed to the cytosol by an OMA1-DELE1-HRI pathway. *Nature* 579: 427-432

Hao Z, Liu L, Tao Z, Wang R, Ren H, Sun H, Lin Z, Zhang Z, Mu C, Zhou J *et al* (2019) Motor dysfunction and neurodegeneration in a C9orf72 mouse line expressing poly-PR. *Nat Commun* 10: 2906

Hardiman O, Al-Chalabi A, Chio A, Corr EM, Logroscino G, Robberecht W, Shaw PJ, Simmons Z, van den Berg LH (2017) Amyotrophic lateral sclerosis. *Nat Rev Dis Primers* 3

Jensen BK, Schuldi MH, McAvoy K, Russell KA, Boehringer A, Curran BM, Krishnamurthy K, Wen X, Westergard T, Ma L *et al* (2020) Synaptic dysfunction induced by glycine-alanine dipeptides in C9orf72-ALS/FTD is rescued by SV2 replenishment. *EMBO Mol Med* 12: e10722

Kinch MS, Umlauf S, Plummer M (2015) An analysis of FDA-approved drugs for metabolic diseases. *Drug Discov Today* 20: 648-651

Kwon I, Xiang S, Kato M, Wu L, Theodoropoulos P, Wang T, Kim J, Yun J, Xie Y, McKnight SL (2014) Poly-dipeptides encoded by the C9orf72 repeats bind nucleoli, impede RNA biogenesis, and kill cells. *Science* 345: 1139-1145

Leprivier G, Rotblat B (2020) How does mTOR sense glucose starvation? AMPK is the usual suspect. *Cell Death Discov* 6: 27

Li S, Wu Z, Li Y, Tantray I, De Stefani D, Mattarei A, Krishnan G, Gao FB, Vogel H, Lu B (2020) Altered MICOS Morphology and Mitochondrial Ion Homeostasis Contribute to Poly(GR) Toxicity Associated with C9-ALS/FTD. *Cell Rep* 32: 107989

Li X, Valencia A, McClory H, Sapp E, Kegel KB, Difiglia M (2012) Deficient Rab11 activity underlies glucose hypometabolism in primary neurons of Huntington's disease mice. *Biochem Biophys Res Commun* 421: 727-730

Lopez-Gonzalez R, Lu Y, Gendron TF, Karydas A, Tran H, Yang D, Petrucelli L, Miller BL, Almeida S, Gao FB (2016) Poly(GR) in C9ORF72-Related ALS/FTD Compromises Mitochondrial Function and Increases Oxidative Stress and DNA Damage in iPSC-Derived Motor Neurons. *Neuron* 92: 383-391

Ludolph AC, Dorst J, Dreyhaupt J, Weishaupt JH, Kassubek J, Weiland U, Meyer T, Petri S, Hermann A, Emmer A *et al* (2020) Effect of High-Caloric Nutrition on Survival in Amyotrophic Lateral Sclerosis. *Ann Neurol* 87: 206-216

Masrori P, Van Damme P (2020) Amyotrophic lateral sclerosis: a clinical review. *Eur J Neurol* 27: 1918-1929

May S, Hornburg D, Schludi MH, Arzberger T, Rentzsch K, Schwenk BM, Grasser FA, Mori K, Kremmer E, Banzhaf-Strathmann J *et al* (2014) C9orf72 FTLD/ALS-associated Gly-Ala dipeptide repeat proteins cause neuronal toxicity and Unc119 sequestration. *Acta Neuropathol* 128: 485-503

Mori K, Arzberger T, Grasser FA, Gijselinck I, May S, Rentzsch K, Weng SM, Schludi MH, van der Zee J, Cruts M *et al* (2013) Bidirectional transcripts of the expanded C9orf72 hexanucleotide repeat are translated into aggregating dipeptide repeat proteins. *Acta Neuropathol* 126: 881-893

Nelson AT, Trotti D (2022) Altered Bioenergetics and Metabolic Homeostasis in Amyotrophic Lateral Sclerosis. *Neurotherapeutics* 19: 1102-1118

O'Connor T, Sadleir KR, Maus E, Velliquette RA, Zhao J, Cole SL, Eimer WA, Hitt B, Bembinster LA, Lammich S *et al* (2008) Phosphorylation of the translation initiation factor eIF2alpha increases BACE1 levels and promotes amyloidogenesis. *Neuron* 60: 988-1009

O'Rourke JG, Bogdanik L, Muhammad A, Gendron TF, Kim KJ, Austin A, Cady J, Liu EY, Zarrow J, Grant S *et al* (2015) C9orf72 BAC Transgenic Mice Display Typical Pathologic Features of ALS/FTD. *Neuron* 88: 892-901

Paganoni S, Macklin EA, Hendrix S, Berry JD, Elliott MA, Maiser S, Karam C, Caress JB, Owegi MA, Quick A *et al* (2020) Trial of Sodium Phenylbutyrate-Taurursodiol for Amyotrophic Lateral Sclerosis. *N Engl J Med* 383: 919-930

Pakos-Zebrucka K, Koryga I, Mnich K, Ljujic M, Samali A, Gorman AM (2016) The integrated stress response. *EMBO Rep* 17: 1374-1395

Pan Y, Kagawa Y, Sun J, Turner BJ, Huang C, Shah AD, Schittenhelm RB, Nicolazzo JA (2022) Altered Blood-Brain Barrier Dynamics in the C9orf72 Hexanucleotide Repeat Expansion Mouse Model of Amyotrophic Lateral Sclerosis. *Pharmaceutics* 14

Pang Z, Chong J, Zhou G, de Lima Morais DA, Chang L, Barrette M, Gauthier C, Jacques PE, Li S, Xia J (2021) MetaboAnalyst 5.0: narrowing the gap between raw spectra and functional insights. *Nucleic Acids Res* 49: W388-W396

Popuri K, Beg MF, Lee H, Balachandar R, Wang L, Sossi V, Jacova C, Baker M, Shahinfard E, Rademakers R *et al* (2021) FDG-PET in presymptomatic C9orf72 mutation carriers. *Neuroimage Clin* 31: 102687

Prapong T, Buss J, Hsu WH, Heine P, West Greenlee H, Uemura E (2002) Amyloid beta-peptide decreases neuronal glucose uptake despite causing increase in GLUT3 mRNA transcription and GLUT3 translocation to the plasma membrane. *Exp Neurol* 174: 253-258

Renton AE, Majounie E, Waite A, Simon-Sanchez J, Rollinson S, Gibbs JR, Schymick JC, Laaksovirta H, van Swieten JC, Myllykangas L *et al* (2011) A hexanucleotide repeat expansion in C9ORF72 is the cause of chromosome 9p21-linked ALS-FTD. *Neuron* 72: 257-268

Schludi MH, May S, Grasser FA, Rentzsch K, Kremmer E, Kupper C, Klopstock T, German Consortium for Frontotemporal Lobar D, Bavarian Brain Banking A, Arzberger T *et al* (2015) Distribution of dipeptide repeat proteins in cellular models and C9orf72 mutation cases suggests link to transcriptional silencing. *Acta Neuropathol* 130: 537-555

Smith EF, Shaw PJ, De Vos KJ (2019) The role of mitochondria in amyotrophic lateral sclerosis. *Neurosci Lett* 710: 132933

Soares R, Ribeiro FF, Xapelli S, Genebra T, Ribeiro MF, Sebastiao AM, Rodrigues CMP, Sola S (2018) Tauroursodeoxycholic Acid Enhances Mitochondrial Biogenesis, Neural Stem Cell Pool, and Early Neurogenesis in Adult Rats. *Mol Neurobiol* 55: 3725-3738

Tabet R, Schaeffer L, Freyermuth F, Jambeau M, Workman M, Lee CZ, Lin CC, Jiang J, Jansen-West K, Abou-Hamdan H *et al* (2018) CUG initiation and frameshifting enable production of dipeptide repeat proteins from ALS/FTD C9ORF72 transcripts. *Nat Commun* 9: 152

Verdone BM, Cicardi ME, Wen X, Sriramoji S, Russell K, Markandaiah SS, Jensen BK, Krishnamurthy K, Haeusler AR, Pasinelli P *et al* (2022) A mouse model with widespread expression of the C9orf72-linked glycine-arginine dipeptide displays non-lethal ALS/FTD-like phenotypes. *Sci Rep* 12: 5644

Wang T, Liu H, Itoh K, Oh S, Zhao L, Murata D, Sesaki H, Hartung T, Na CH, Wang J (2021) C9orf72 regulates energy homeostasis by stabilizing mitochondrial complex I assembly. *Cell Metab* 33: 531-546 e539

Wen X, Tan W, Westergard T, Krishnamurthy K, Markandaiah SS, Shi Y, Lin S, Shneider NA, Monaghan J, Pandey UB *et al* (2014) Antisense proline-arginine RAN dipeptides linked to C9ORF72-ALS/FTD form toxic nuclear aggregates that initiate in vitro and in vivo neuronal death. *Neuron* 84: 1213-1225

Westergard T, McAvoy K, Russell K, Wen X, Pang Y, Morris B, Pasinelli P, Trotti D, Haeusler A (2019) Repeat-associated non-AUG translation in C9orf72-ALS/FTD is driven by neuronal excitation and stress. *EMBO Mol Med* 11

Wu N, Yang M, Gaur U, Xu H, Yao Y, Li D (2016) Alpha-Ketoglutarate: Physiological Functions and Applications. *Biomol Ther (Seoul)* 24: 1-8

Xia K, Witzel S, Witzel C, Klose V, Fan D, Ludolph AC, Dorst J (2023) Mutation-specific metabolic profiles in presymptomatic amyotrophic lateral sclerosis. *Eur J Neurol* 30: 87-95

Xie N, Zhang L, Gao W, Huang C, Huber PE, Zhou X, Li C, Shen G, Zou B (2020) NAD(+) metabolism: pathophysiologic mechanisms and therapeutic potential. *Signal Transduct Target Ther* 5: 227

Yang R, Wek SA, Wek RC (2000) Glucose Limitation Induces GCN4 Translation by Activation of Gcn2 Protein Kinase. *Mol Biol Cell* 20: 2706-2717

Yang YM, Gupta SK, Kim KJ, Powers BE, Cerqueira A, Wainger BJ, Ngo HD, Rosowski KA, Schein PA, Ackeifi CA *et al* (2013) A small molecule screen in stem-cell-derived motor neurons identifies a kinase inhibitor as a candidate therapeutic for ALS. *Cell Stem Cell* 12: 713-726

Zu T, Guo S, Bardhi O, Ryskamp DA, Li J, Khoramian Tusi S, Engelbrecht A, Klippel K, Chakrabarty P, Nguyen L *et al* (2020) Metformin inhibits RAN translation through PKR pathway and mitigates disease in C9orf72 ALS/FTD mice. *Proc Natl Acad Sci U S A* 117: 18591-18599

Zu T, Liu Y, Banez-Coronel M, Reid T, Pletnikova O, Lewis J, Miller TM, Harms MB, Falchook AE, Subramony SH *et al* (2013) RAN proteins and RNA foci from antisense transcripts in C9ORF72 ALS and frontotemporal dementia. *Proc Natl Acad Sci U S A* 110: E4968-4977

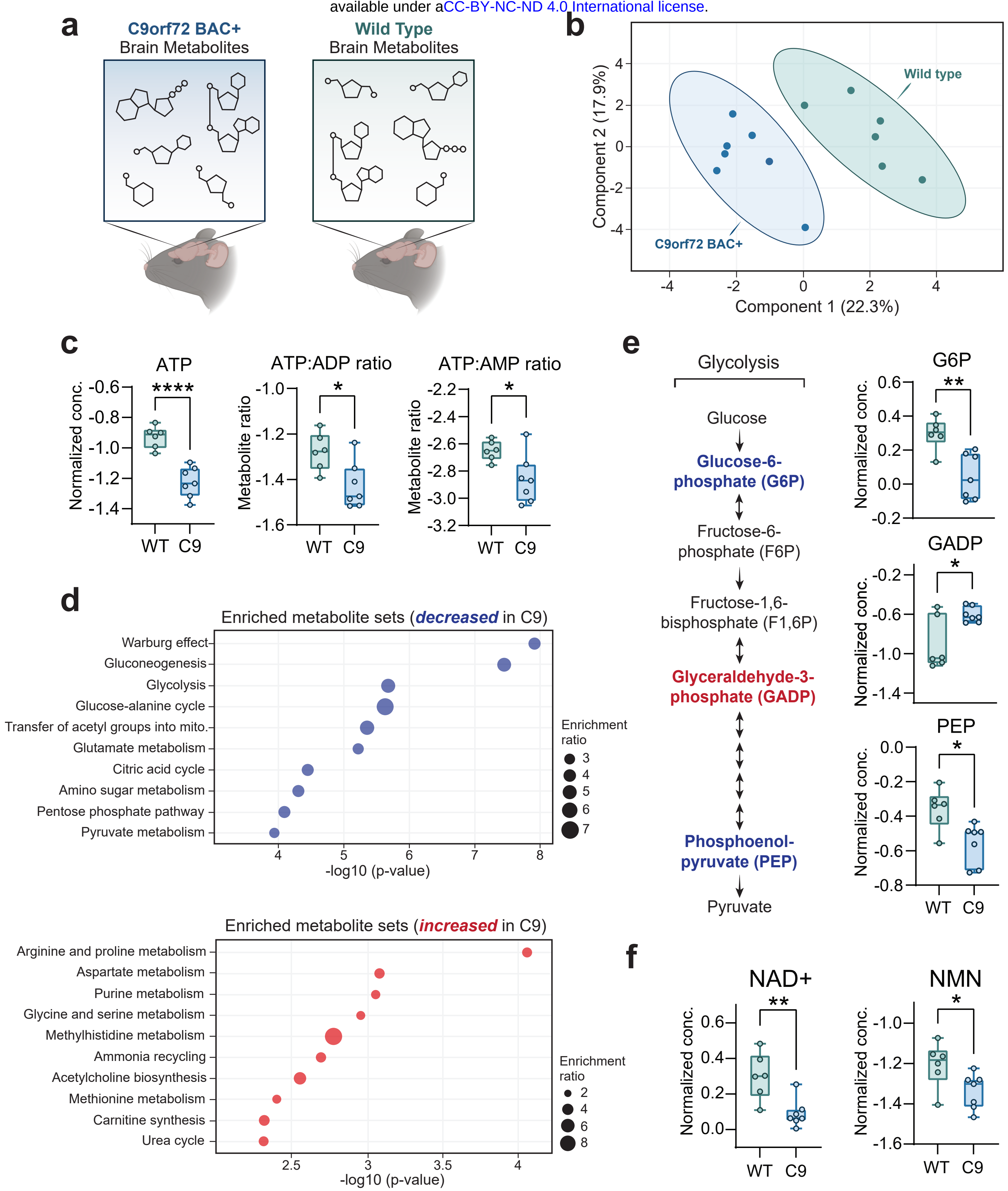
a
C9orf72 BAC+
Brain Metabolites
Wild Type
Brain Metabolites
b
Component 2 (17.9%)
Component 1 (22.3%)
Wild type
C9orf72 BAC+
-4
-2
0
2
4
c
ATP
Normalized conc.
-0.6
-0.8
-1.0
-1.2
-1.4
****
ATP:ADP ratio
Metabolite ratio
-1.0
-1.2
-1.4
-1.6
*
ATP:AMP ratio
Metabolite ratio
-2.2
-2.4
-2.6
-2.8
-3.0
-3.2
*
WT
C9
d
Enriched metabolite sets (*decreased* in C9)
Warburg effect
Gluconeogenesis
Glycolysis
Glucose-alanine cycle
Transfer of acetyl groups into mito.
Glutamate metabolism
Citric acid cycle
Amino sugar metabolism
Pentose phosphate pathway
Pyruvate metabolism
-log10 (p-value)
4
5
6
7
8
Enrichment ratio
3
4
5
6
7
Enriched metabolite sets (*increased* in C9)
Arginine and proline metabolism
Aspartate metabolism
Purine metabolism
Glycine and serine metabolism
Methylhistidine metabolism
Ammonia recycling
Acetylcholine biosynthesis
Methionine metabolism
Carnitine synthesis
Urea cycle
-log10 (p-value)
2.5
3
3.5
4
Enrichment ratio
2
4
6
8
e
Glycolysis
Glucose
Glucose-6-phosphate (G6P)
Fructose-6-phosphate (F6P)
Fructose-1,6-bisphosphate (F1,6P)
Glyceraldehyde-3-phosphate (GADP)
Phosphoenol-pyruvate (PEP)
Pyruvate
G6P
Normalized conc.
0.6
0.4
0.2
0.0
-0.2
**
GADP
Normalized conc.
-0.2
-0.6
-1.0
-1.4
*
PEP
Normalized conc.
0.0
-0.2
-0.4
-0.6
-0.8
*
WT
C9
f
NAD+
Normalized conc.
0.6
0.4
0.2
0.0
**
NMN
Normalized conc.
-1.0
-1.2
-1.4
-1.6
*
WT
C9

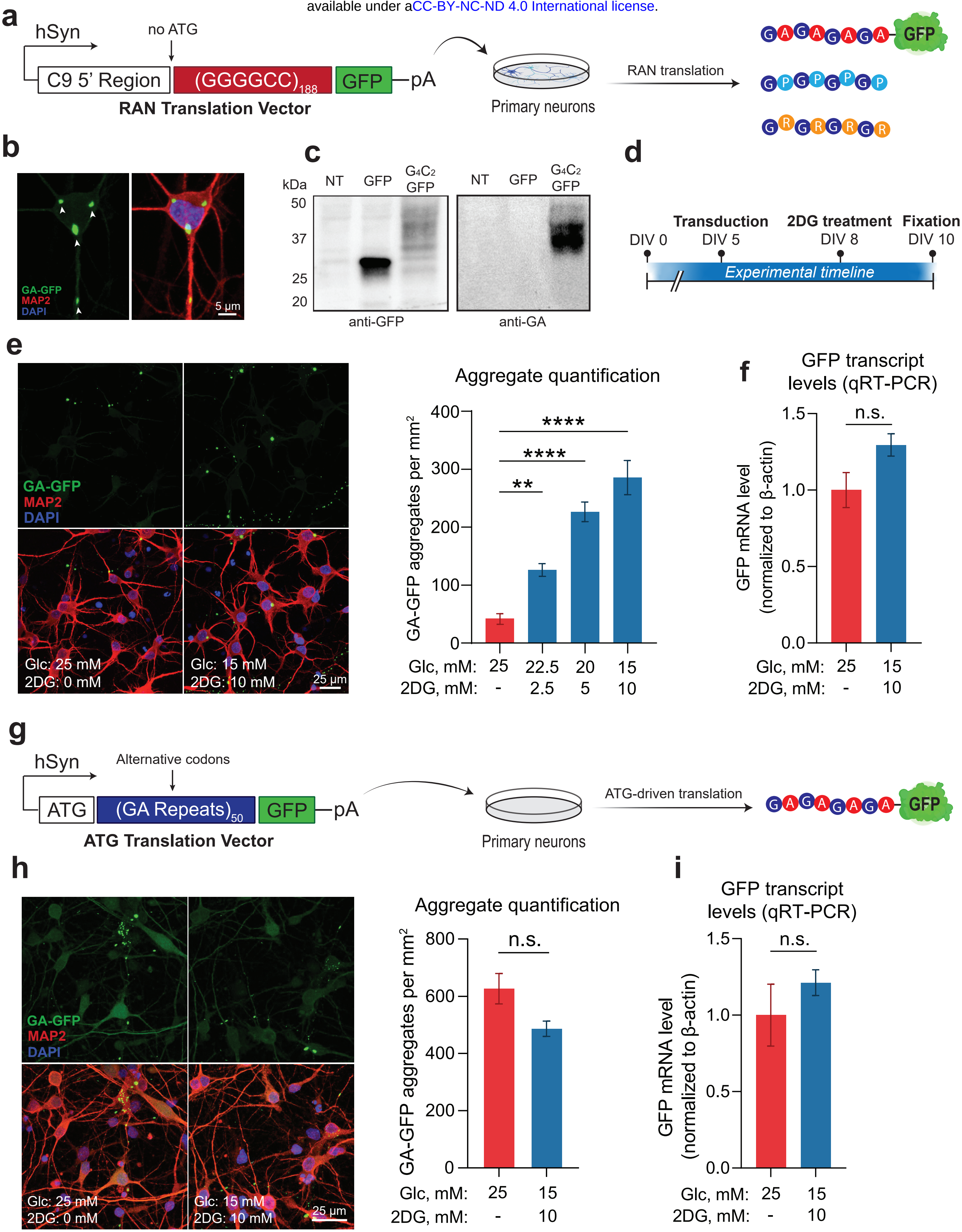
a
hSyn
no ATG
C9 5' Region
(GGGGCC)188
GFP
pA
RAN Translation Vector
Primary neurons
RAN translation
GAGAGAGA GFP
GPGPGPGP
GRGRGRGR
b
GA-GFP
MAP2
DAPI
5 µm
c
kDa
NT
GFP
G4C2 GFP
50
37
25
20
anti-GFP
anti-GA
d
Transduction
2DG treatment
Fixation
DIV 0
DIV 5
DIV 8
DIV 10
Experimental timeline
e
GA-GFP
MAP2
DAPI
Glc: 25 mM
2DG: 0 mM
Glc: 15 mM
2DG: 10 mM
25 µm
Aggregate quantification
GA-GFP aggregates per mm²
400
300
200
100
0
****
****
**
Glc, mM: 25 22.5 20 15
2DG, mM: - 2.5 5 10
f
GFP transcript levels (qRT-PCR)
GFP mRNA level (normalized to β-actin)
1.5
1.0
0.5
0.0
n.s.
Glc, mM: 25 15
2DG, mM: - 10
g
hSyn
Alternative codons
ATG
(GA Repeats)50
GFP
pA
ATG Translation Vector
Primary neurons
ATG-driven translation
GAGAGAGA GFP
h
GA-GFP
MAP2
DAPI
Glc: 25 mM
2DG: 0 mM
Glc: 15 mM
2DG: 10 mM
25 µm
Aggregate quantification
GA-GFP aggregates per mm²
800
600
400
200
0
n.s.
Glc, mM: 25 15
2DG, mM: - 10
i
GFP transcript levels (qRT-PCR)
GFP mRNA level (normalized to β-actin)
1.5
1.0
0.5
0.0
n.s.
Glc, mM: 25 15
2DG, mM: - 10

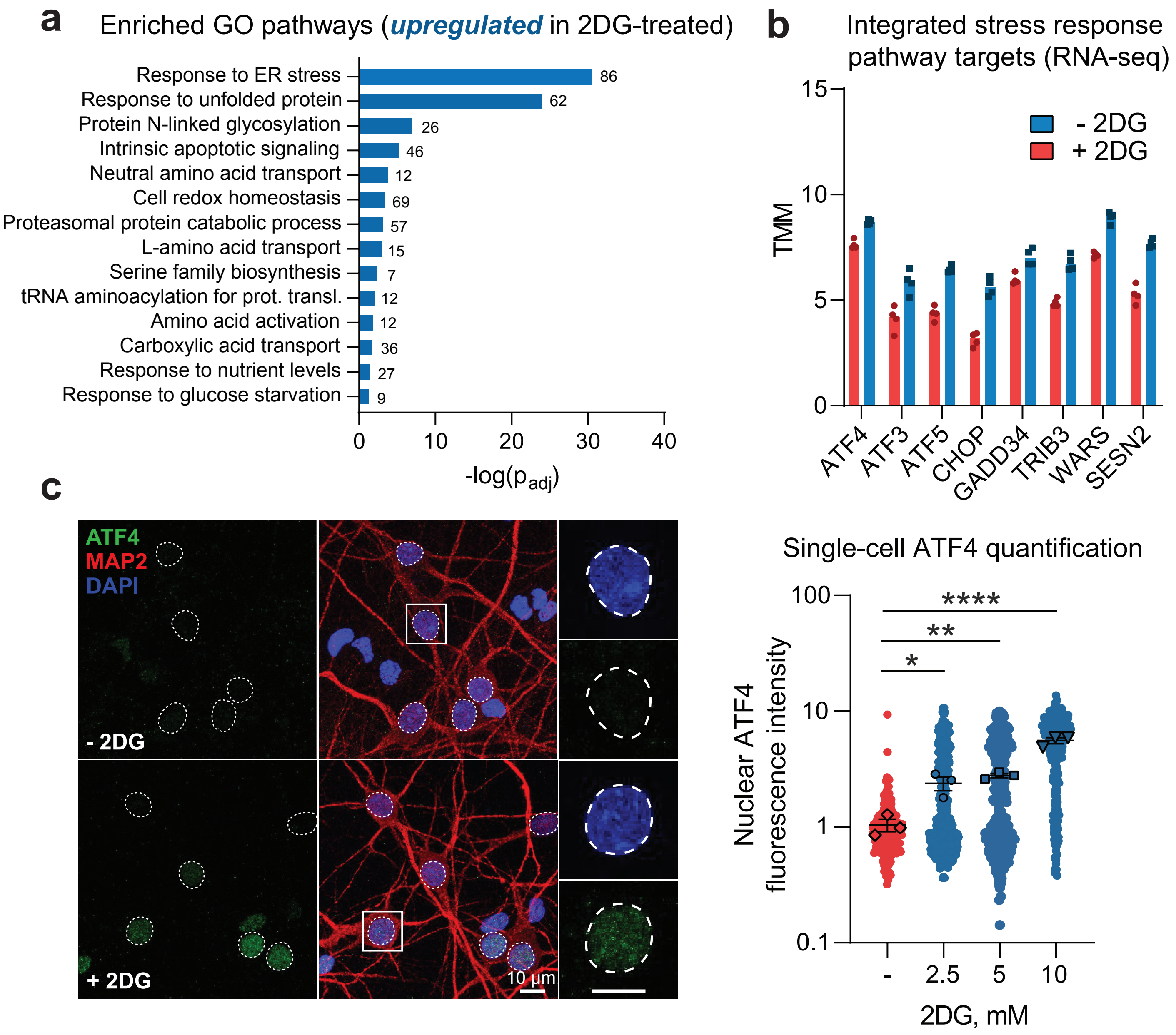
a
Enriched GO pathways (upregulated in 2DG-treated)
Response to ER stress 86
Response to unfolded protein 62
Protein N-linked glycosylation 26
Intrinsic apoptotic signaling 46
Neutral amino acid transport 12
Cell redox homeostasis 69
Proteasomal protein catabolic process 57
L-amino acid transport 15
Serine family biosynthesis 7
tRNA aminoacylation for prot. transl. 12
Amino acid activation 12
Carboxylic acid transport 36
Response to nutrient levels 27
Response to glucose starvation 9
0
10
20
30
40
-log(p_adj)
b
Integrated stress response pathway targets (RNA-seq)
15
10
5
0
TMM
- 2DG
+ 2DG
ATF4
ATF3
ATF5
CHOP
GADD34
TRIB3
WARS
SESN2
c
ATF4
MAP2
DAPI
- 2DG
+ 2DG
10 µm
Single-cell ATF4 quantification
100
10
1
0.1
Nuclear ATF4 fluorescence intensity
****
**
*
-
2.5
5
10
2DG, mM

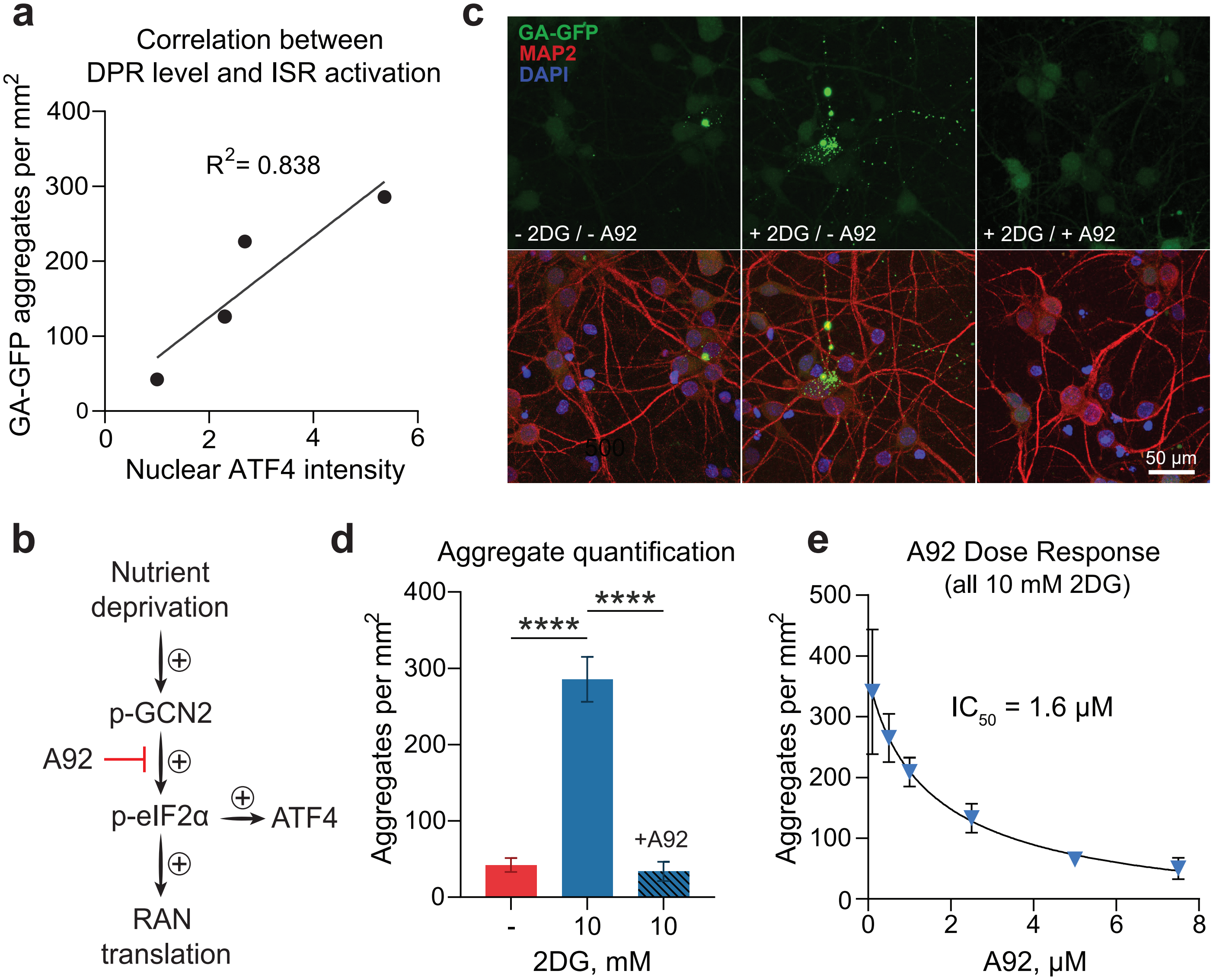
a
Correlation between DPR level and ISR activation
GA-GFP aggregates per mm²
400
300
200
100
0
R² = 0.838
0
2
4
6
Nuclear ATF4 intensity
c
GA-GFP
MAP2
DAPI
- 2DG / - A92
+ 2DG / - A92
+ 2DG / + A92
500
50 µm
b
Nutrient deprivation
⊕
p-GCN2
A92
⊕
p-eIF2α
⊕
ATF4
⊕
RAN translation
d
Aggregate quantification
Aggregates per mm²
400
300
200
100
0
****
****
+A92
-
10
10
2DG, mM
e
A92 Dose Response
(all 10 mM 2DG)
Aggregates per mm²
500
400
300
200
100
0
IC50 = 1.6 µM
0
2
4
6
8
A92, µM

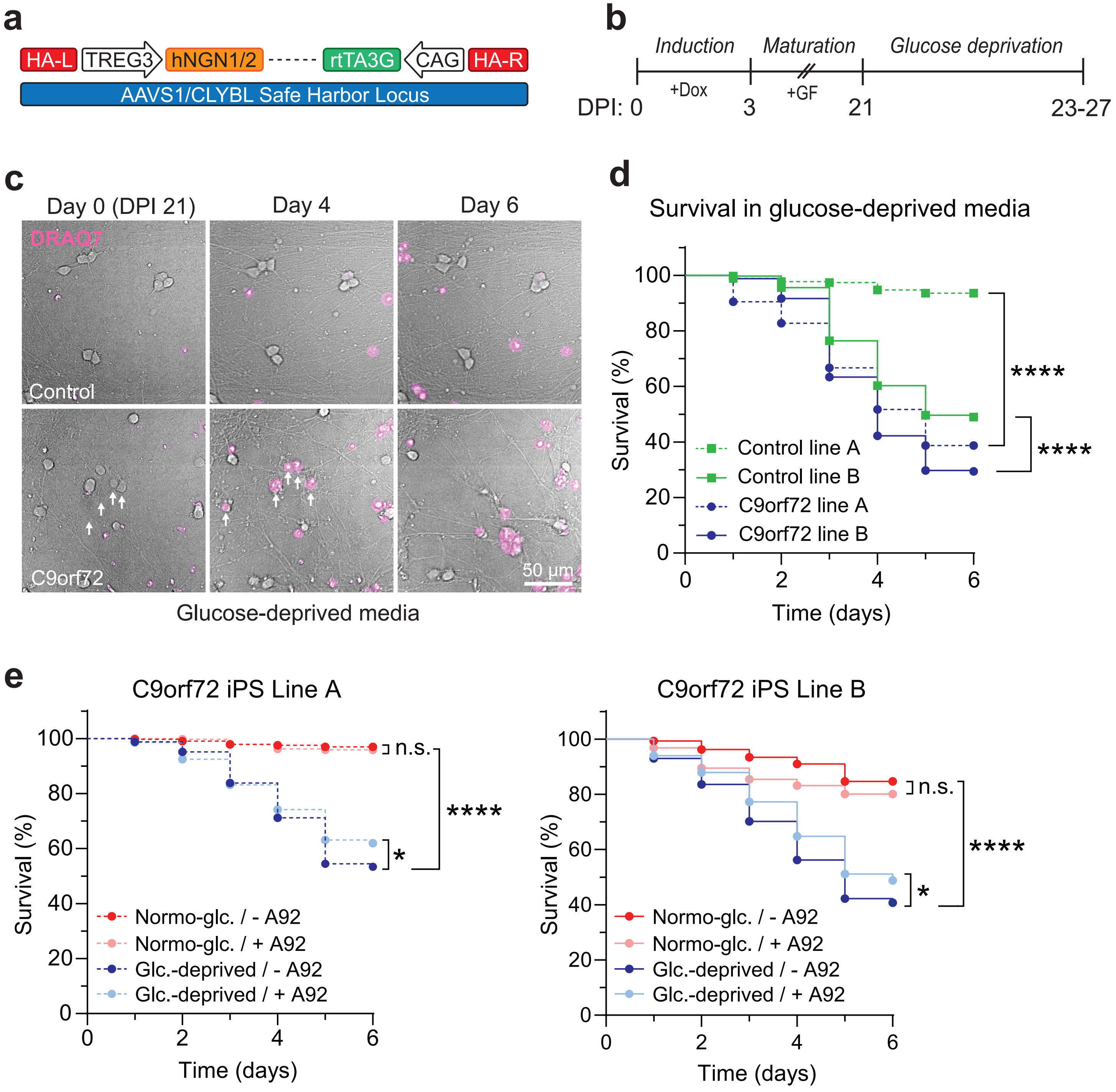
a
HA-L
TREG3
hNGN1/2
rtTA3G
CAG
HA-R
AAVS1/CLYBL Safe Harbor Locus
b
Induction
Maturation
Glucose deprivation
+Dox
+GF
DPI: 0
3
21
23-27
c
Day 0 (DPI 21)
Day 4
Day 6
DRAQ7
Control
C9orf72
50 μm
Glucose-deprived media
d
Survival in glucose-deprived media
Survival (%)
Time (days)
Control line A
Control line B
C9orf72 line A
C9orf72 line B
****
****
e
C9orf72 iPS Line A
C9orf72 iPS Line B
Survival (%)
Time (days)
Normo-glc. / - A92
Normo-glc. / + A92
Glc.-deprived / - A92
Glc.-deprived / + A92
n.s.
****
*

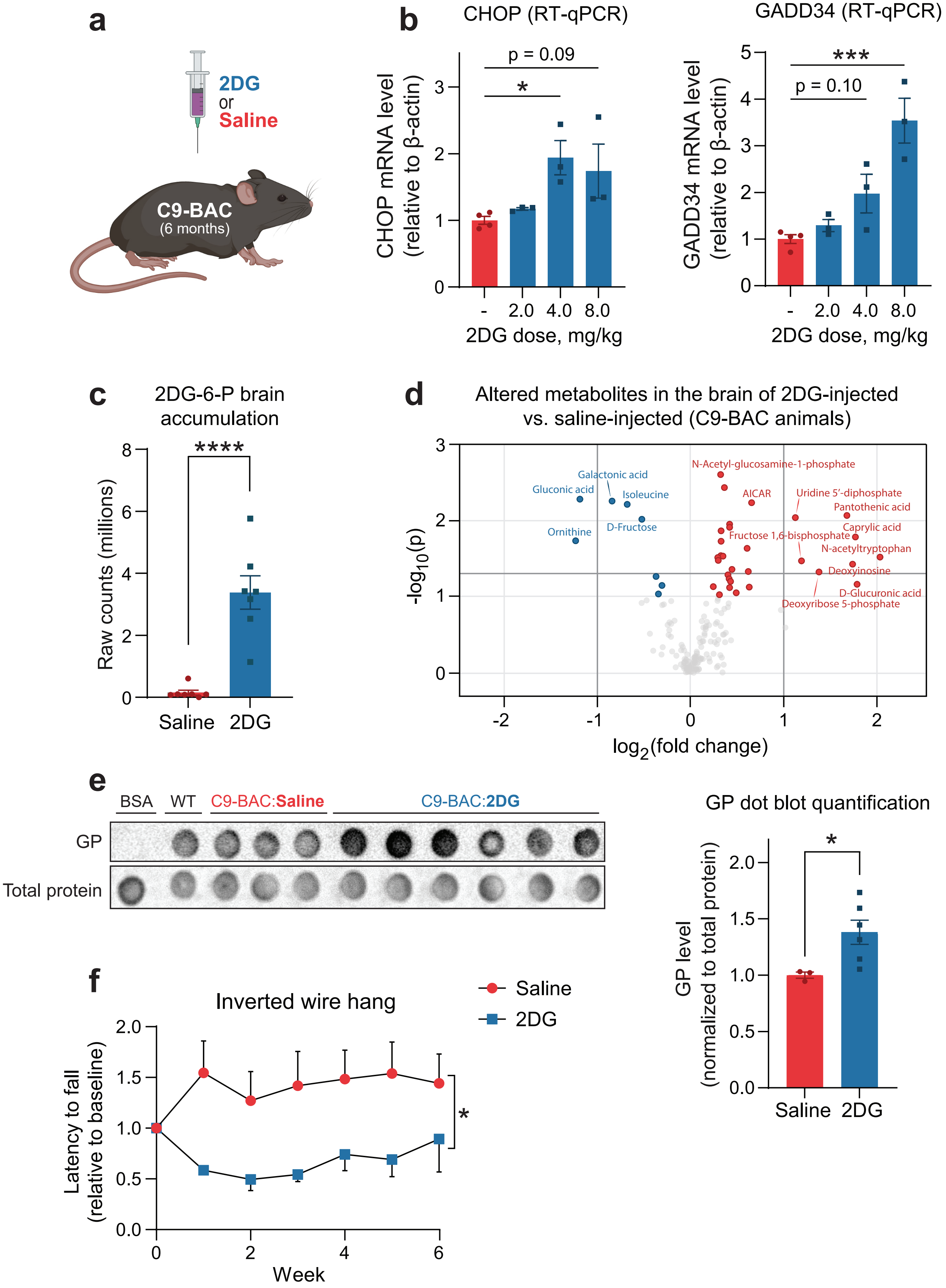
a
2DG
or
Saline
C9-BAC
(6 months)
b
CHOP (RT-qPCR)
CHOP mRNA level
(relative to β-actin)
p = 0.09
*
0
1
2
3
-
2.0
4.0
8.0
2DG dose, mg/kg
GADD34 (RT-qPCR)
GADD34 mRNA level
(relative to β-actin)
***
p = 0.10
0
1
2
3
4
5
-
2.0
4.0
8.0
2DG dose, mg/kg
c
2DG-6-P brain accumulation
Raw counts (millions)
****
0
2
4
6
8
Saline
2DG
d
Altered metabolites in the brain of 2DG-injected vs. saline-injected (C9-BAC animals)
-log10(p)
log2(fold change)
Galactonic acid
Gluconic acid
Isoleucine
Ornithine
D-Fructose
N-Acetyl-glucosamine-1-phosphate
AICAR
Uridine 5'-diphosphate
Pantothenic acid
Caprylic acid
Fructose 1,6-bisphosphate
N-acetyltryptophan
Deoxyinosine
D-Glucuronic acid
Deoxyribose 5-phosphate
0
1
2
3
-2
-1
0
1
2
e
BSA
WT
C9-BAC:Saline
C9-BAC:2DG
GP
Total protein
GP dot blot quantification
GP level
(normalized to total protein)
*
0.0
0.5
1.0
1.5
2.0
Saline
2DG
f
Inverted wire hang
Saline
2DG
Latency to fall
(relative to baseline)
*
0.0
0.5
1.0
1.5
2.0
0
2
4
6
Week

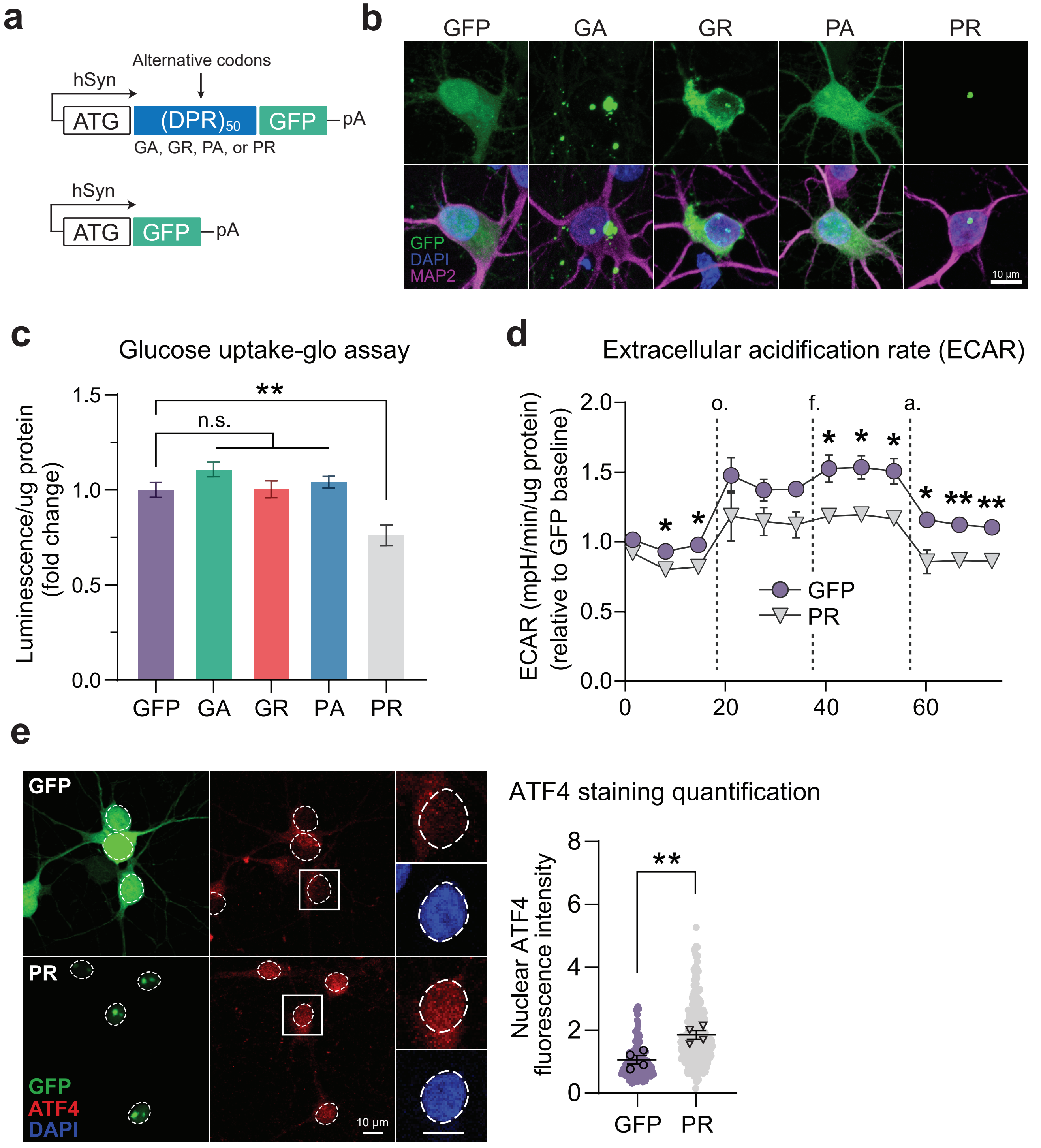
a
Alternative codons
hSyn
ATG
(DPR)$_{50}$
GFP
pA
GA, GR, PA, or PR
hSyn
ATG
GFP
pA
b
GFP
GA
GR
PA
PR
GFP
DAPI
MAP2
10 µm
c
Glucose uptake-glo assay
Luminescence/ug protein (fold change)
1.5
1.0
0.5
0.0
**
n.s.
GFP
GA
GR
PA
PR
d
Extracellular acidification rate (ECAR)
ECAR (mpH/min/ug protein) (relative to GFP baseline)
2.0
1.5
1.0
0.5
0.0
o.
f.
a.
*
*
*
*
*
*
**
**
GFP
PR
0
20
40
60
e
GFP
PR
GFP
ATF4
DAPI
10 µm
ATF4 staining quantification
Nuclear ATF4 fluorescence intensity
8
6
4
2
0
**
GFP
PR

	Fold change	log2(Fold change)	p-value
2DGP	17.747	4.1495	0.000
N-Acetyl-glucosamine 1-phosphate	1.2507	0.32277	0.002
D-Ribulose 5-phosphate	1.2862	0.36312	0.004
Gluconic acid	0.43964	-1.1856	0.005
Galactonic acid	0.5579	-0.84192	0.006
AICAR	1.5763	0.65655	0.006
L-Isoleucine	0.62487	-0.67837	0.006
Pantothenic acid	3.2048	1.6802	0.009
Uridine 5'-diphosphate	2.1806	1.1247	0.009
D-Fructose	0.69694	-0.5209	0.010
N-Acetyl-D-glucosamine	1.3384	0.42056	0.011
Uracil	1.3381	0.42016	0.012
L-Methionine	1.2566	0.32948	0.014
Caprylic acid	3.4104	1.7699	0.016
Ornithine	0.42576	-1.2319	0.018
Riboflavin	1.2559	0.32874	0.019
N6-Acetyl-L-lysine	1.5243	0.60817	0.023
Choline	1.2534	0.32586	0.029
L-Serine	1.2737	0.34907	0.029
N-acetyltryptophan	4.0996	2.0355	0.030
Uridine diphosphate-N-acetylglucosamine	1.2244	0.2921	0.031
Uridine 5'-monophosphate	1.2292	0.29771	0.033
Fructose 1,6-bisphosphate	2.2852	1.1923	0.034
Deoxyinosine	3.3378	1.7389	0.037
Isovalerylcarnitine	1.3607	0.44438	0.044
2-Hydroxycaproic acid	1.5378	0.62091	0.046
Deoxyribose 5-phosphate	2.6036	1.3805	0.047
Deoxyuridine	1.3224	0.40315	0.051
Xanthine	0.77474	-0.36821	0.054
L-Phenylalanine	1.3329	0.41462	0.058
Imidazoleacetic acid	1.3465	0.42924	0.063
D-Glucuronic acid	3.4526	1.7877	0.068
Phosphorylcholine	0.80966	-0.30461	0.071
N-Acetyl-L-alanine	1.1848	0.24459	0.073
4-Trimethylammoniobutanoic acid	1.549	0.63133	0.075
Thymine	1.3379	0.41996	0.076
Thymidine	1.4051	0.49068	0.088
N-Acetylasparagine	0.78788	-0.34396	0.092
L-Tyrosine	1.2395	0.30981	0.093

(in order of significance)